Amoxicillin-resistant *Streptococcus pneumoniae* can be resensitized by targeting the mevalonate pathway as indicated by sCRilecs-seq

Liselot Dewachter[a], Xue Liu[a,b], Julien Dénéréaz[a], Vincent de Bakker[a], Charlotte Costa[c], Mara Baldry[c], Jean-Claude Sirard[c], Jan-Willem Veening[a]*

[a] Department of Fundamental Microbiology, Faculty of Biology and Medicine, University of Lausanne, Biophore Building, Lausanne 1015, Switzerland

[b] Guangdong Key Laboratory for Genome Stability and Human Disease Prevention, Department of Pharmacology, International Cancer Center, Shenzhen University Health Science Center, 518060 Shenzhen, China

[c] Univ. Lille, CNRS, Inserm, CHU Lille, Institut Pasteur Lille, U1019 - UMR 9017 - CIIL - Center for Infection and Immunity of Lille, F-59000 Lille, France

*Correspondence to: jan-willem.veening@unil.ch Twitter: @JWVeening

Abstract

Antibiotic resistance in the important opportunistic human pathogen *Streptococcus pneumoniae* is on the rise. This is particularly problematic in the case of the β-lactam antibiotic amoxicillin, which is the first-line therapy. It is therefore crucial to uncover targets that would kill or resensitize amoxicillin-resistant pneumococci. To do so, we developed a genome-wide, single-cell based, gene silencing screen using CRISPR interference called sCRilecs-seq (subsets of CRISPR interference libraries extracted by fluorescence activated cell sorting coupled to next generation sequencing). Since amoxicillin affects growth and division, sCRilecs-seq was used to identify targets that are responsible for maintaining proper cell size. Our screen revealed that downregulation of the mevalonate pathway leads to extensive cell elongation. Further investigation into this phenotype indicates that it is caused by insufficient transport of cell wall precursors across the cell membrane due to a limitation in the production of undecaprenyl phosphate (Und-P), the lipid carrier responsible for this process. The data suggest that whereas peptidoglycan synthesis continues even with reduced Und-P levels, cell constriction is specifically halted. We successfully exploited this knowledge to create a combination treatment strategy where the FDA-approved drug clomiphene, an inhibitor of Und-P synthesis, is paired up with amoxicillin. Our results show that clomiphene potentiates the antimicrobial activity of amoxicillin and that combination therapy resensitizes amoxicillin-resistant *S. pneumoniae*. These findings could provide a starting point to develop a solution for the increasing amount of hard-to-treat amoxicillin-resistant pneumococcal infections.

Keywords

sCRilecs-seq, mevalonate pathway, morphology, peptidoglycan synthesis, cell division, antibiotic resistance, amoxicillin, clomiphene, combination therapy

40 **Introduction**

41 *Streptococcus pneumoniae* (the pneumococcus) is an opportunistic human pathogen that is responsible
42 for diseases such as pneumonia, middle ear infections, sepsis and meningitis[1-3]. *S. pneumoniae* is listed by
43 the WHO as a priority pathogen for the development of novel antibiotics, since it is one of the leading
44 causes of fatal bacterial infections worldwide[1,2,4] and antibiotic resistance is on the rise[5-7]. The alarming
45 increase in prevalence of penicillin non-susceptible *S. pneumoniae* was initially dealt with by the
46 development and roll-out of the pneumococcal conjugate vaccines PCV7, PCV10 and PCV13 in 2001, 2009
47 and 2010, respectively[5]. These vaccines induce protection against infection caused by 7, 10 or 13 of the
48 most prevalent serotypes of capsular polysaccharides that surround *S. pneumoniae*[3]. Since many of the
49 targeted serotypes are associated with penicillin non-susceptibility, the occurrence of infections with such
50 resistant strains decreased at first[5,8,9]. However, due to the high genomic plasticity of *S. pneumoniae*[10,11],
51 serotype switching created penicillin non-susceptible escape mutants that are not covered by the
52 currently available vaccines and that are once again gaining in prevalence[5,8].

53

54 Penicillin non-susceptible *S. pneumoniae* strains carry a variety of mutations in their penicillin binding
55 proteins (PBPs) that decrease their affinity for penicillin and therefore increase resistance[4,7,12]. These
56 mutations do not only lower the susceptibility to penicillin but also to other β-lactam antibiotics[13].
57 However, the efficacy of aminopenicillins such as amoxicillin is usually less affected by these mutations,
58 meaning that amoxicillin remains a viable treatment option for many penicillin non-susceptible strains
59 and therefore became one of the frontline antibiotics to treat pneumococcal infections[13-17]. However,
60 highly penicillin resistant strains have been found to also be amoxicillin non-susceptible[5,6], thereby now
61 also threatening the clinical efficacy of this widely used antibiotic.

62

63 Because of the rise in antibiotic resistance, we urgently need new antibiotic targets and/or need to find
64 ways to extend the clinical efficacy of our current antibiotic arsenal. To contribute towards this goal, we
65 developed sCRilecs-seq (subsets of CRISPR interference libraries extracted by fluorescence activated cell
66 sorting coupled to next generation sequencing), a high-throughput single-cell based screening approach
67 that we exploited to find targets that could resensitize resistant *S. pneumoniae* strains towards amoxicillin.
68 sCRilecs-seq is based upon genome-wide gene silencing using CRISPR interference (CRISPRi), which makes
69 use of a catalytically dead form of the Cas9 enzyme, called dCas9[18]. dCas9 is guided towards its target site
70 in the DNA by the provided sgRNA but is unable to introduce double-stranded breaks. Instead, the dCas9
71 enzyme acts as a roadblock for RNA polymerase, thereby halting transcription[18-20]. CRISPRi gene silencing

72 not only affects the target gene but influences the expression of an entire transcriptional unit[18-22]. This
73 technology therefore works at the operon level and generates strong polar effects that need to be
74 considered. Despite this limitation, CRISPRi has proven to be a very powerful genetic tool to perform
75 genome-wide depletion screens in various bacteria[22-27]. In the sCRilecs-seq screen used here,
76 subpopulations that display a phenotype of interest are collected using Fluorescence Activated Cell
77 Sorting (FACS), as has previously been done in eukaryotic cells[28] and for bacterial transposon libraries[29].
78 The abundance of sgRNAs in the sorted fractions are then compared to a defined control population to
79 look for genetic factors involved in the phenotype of interest. This highly flexible screening approach
80 allowed us to identify targets that can be exploited in our fight against bacterial infections.
81
82 Our sCRilecs-seq results highlight the importance of the mevalonate pathway for maintaining proper cell
83 morphology in *S. pneumoniae*. The mevalonate pathway is the only pathway used by *S. pneumoniae* to
84 produce isoprenoids, a highly diverse class of organic molecules that are essential to all life on earth and
85 that function – among others – in processes such as cell wall synthesis, electron transport, membrane
86 stability and protein modification[30,31]. Our screen revealed that inhibition of the mevalonate pathway in
87 *S. pneumoniae* leads to extensive cell elongation. The data suggests that this elongation is caused by
88 insufficient transport of cell wall precursors across the cell membrane due to a limitation in the production
89 of undecaprenyl phosphate (Und-P), the lipid carrier responsible for this process[32]. This shortage of
90 peptidoglycan precursors allows cell elongation to continue but causes a block in cell division.
91
92 Additionally, based on the mevalonate depletion phenotype characterized here, we successfully designed
93 a combination treatment strategy targeting *S. pneumoniae*. In this combination treatment strategy,
94 amoxicillin is potentiated by the simultaneous administration of clomiphene, a widely used FDA-approved
95 fertility drug that was shown to block Und-P production in *Staphylococcus aureus* and to synergize with
96 β-lactam antibiotics[33]. This combination of compounds is particularly powerful against amoxicillin-
97 resistant *S. pneumoniae* strains, as it is capable of resensitizing these strains to clinically-relevant
98 concentrations of amoxicillin *in vitro*. Our findings could therefore provide a useful starting point for the
99 development of treatment strategies that are effective against the rising amount of amoxicillin-resistant
100 *S. pneumoniae* infections and could extend the clinical efficacy of this important antibiotic.
101

102 **Results**

103 **Amoxicillin treated *S. pneumoniae* are elongated**

104 To identify new druggable pathways that could potentiate the antimicrobial activity of amoxicillin, we first
105 established the impact of amoxicillin on pneumococcal morphology and growth. We therefore performed
106 time-lapse microscopy of *S. pneumoniae* in the presence or absence of amoxicillin. As shown in Figure 1A-
107 B and Movie S1-2, amoxicillin-treated cells initially elongate before they lyse. Indeed, quantitative image
108 analysis confirmed that amoxicillin, like some other β-lactam antibiotics[34], causes cell elongation (Figure
109 1C), while growth curves in the presence of this antibiotic demonstrate that lysis occurs since OD values
110 decrease at high amoxicillin concentrations (Figure 1D). To demonstrate that cell elongation is specifically
111 caused by amoxicillin and does not generally occur upon antibiotic treatment, we also assessed cell
112 lengths in the presence of the fluoroquinolone ciprofloxacin. As expected, ciprofloxacin did not induce
113 cell elongation[35] (Figure 1C). Because it was shown that synergy between antimicrobial compounds is
114 most often detected when they target the same process[36], we hypothesized that targets whose inhibition
115 would cause cell elongation, like amoxicillin, could potentially reinforce the antibacterial effect of this
116 antibiotic.

117

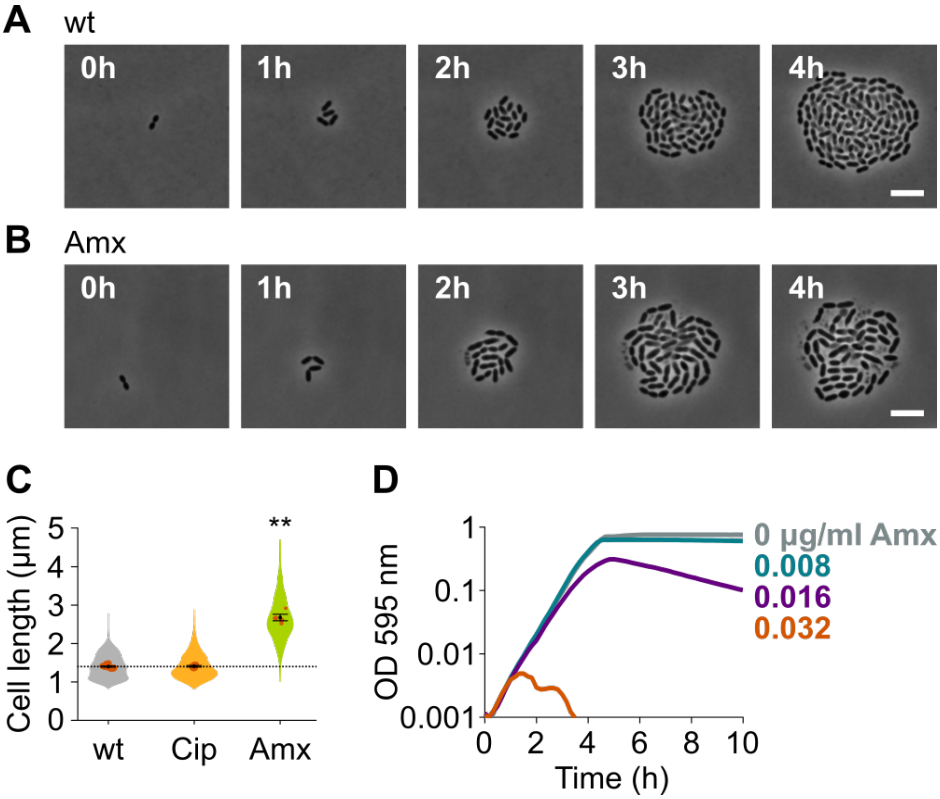

118

119 **Figure 1: Amoxicillin causes cell elongation before triggering cell lysis.** A) Snapshots of a time lapse phase contrast microscopy
120 experiment of *S. pneumoniae* D39V growing in the absence of antibiotics (Movie S1). B) Snapshots of a time lapse analysis of *S.*
121 *pneumoniae* D39V growing in the presence of a sub-MIC concentration of amoxicillin (0.016 µg/ml) (Movie S2). C) The effect of
122 sub-MIC concentrations of ciprofloxacin (0.5 µg/ml) and amoxicillin (0.016 µg/ml) on the cell length of *S. pneumoniae* D39V was
123 tested by phase contrast microscopy after 2h of treatment. Quantitative analysis of micrographs show that cell length increases
124 upon treatment with amoxicillin. Data are represented as violin plots with the mean cell length of every biological repeat indicated
125 with orange dots. The size of these dots indicates the number of cells recorded in each repeat, ranging from 112 to 1498 cells.
126 Black dots represent the mean ± SEM of all recorded means, $n \geq 3$. Two-sided Wilcoxon signed rank tests were performed against
127 wt without antibiotic as control group (dotted line) and p values were adjusted with an FDR correction; ** $p < 0.01$. D) *S.*
128 *pneumoniae* D39V was grown in the presence of different concentrations of amoxicillin and growth was followed by monitoring
129 OD 595 nm. Wt, wildtype; Cip, ciprofloxacin; Amx, amoxicillin.
130

131 **Development of sCRilecs-seq**

132 To identify pathways that lead to cell elongation upon inhibition, we developed a single-cell based, high-
133 throughput screening strategy where we combined CRISPRi gene silencing with high-throughput selection
134 of a phenotype of interest by Fluorescence Activated Cell Sorting (FACS). Using this approach, which we
135 call sCRilecs-seq, we screened for mutants that display an increase in forward scatter (FSC), which is a
136 rough indicator of cell size[37]. To facilitate downstream analyses, screening was performed in a *S.*
137 *pneumoniae* strain in which the DNA and the cell division protein FtsZ are marked. DNA was visualized
138 using the DNA-binding protein HlpA fused to GFP. HlpA, also known as HU, is a histone-like protein that
139 binds DNA aspecifically and is highly expressed in *S. pneumoniae*[38]. It is therefore often used as a nucleoid
140 marker[38,39]. FtsZ was marked by fusing it to mCherry. To this end, the native *hlpA* and *ftsZ* genes of *S.*
141 *pneumoniae* D39V were replaced by *hlpA-gfp* and *ftsZ-mCherry*, respectively. Both of these fusions were
142 previously shown to support viability[38,39]. Additionally, the gene encoding dCas9 was inserted into the
143 pneumococcal chromosome and was placed under tight control of an IPTG-inducible P_{lac} promoter[21,23].
144 The resulting strain (VL3117: D39V *lacI* P_{lac}-*dcas9 hlpA-gfp ftsZ-mCherry*) was transformed with a pool of
145 1499 different integrative plasmids carrying constitutively-expressed sgRNAs (under control of the P3
146 promoter) that together target the entire coding genome[23]. This way, we created a pooled CRISPRi library
147 where each cell expresses a certain sgRNA resulting in transcriptional downregulation of a specific gene
148 or operon upon induction of dCas9 (Figure 2A). Note that sgRNAs were designed in such a way that the
149 chance for off targeting effects are minimal[23].
150

151 We next grew the library in C+Y medium at 37°C for 3.5h in the presence of 1 mM IPTG to induce dCas9.
152 The pooled and induced library was subjected to FACS and different fractions of the population were

153 sorted (see Materials and Methods). Of note, *S. pneumoniae* grows as short cell chains[40] and the number
154 of cells present in a chain could influence the FSC read-out. To ensure that measurements were taken at
155 the single-cell level, chains were mechanically disrupted by vigorous vortexing before sorting took place.
156 We confirmed that this approach is successful at breaking up cell chains ensuring that morphology was
157 evaluated for single cells rather than entire chains (Figure S1A-C). Ten percent of the population with the
158 highest FSC values was collected. As a control, the centermost 70% of the population was sorted as well.
159 For both collected fractions, sgRNAs were amplified by PCR using primers that contain Illumina adapters
160 (see Materials and Methods). After sequencing, sgRNA read counts were compared between the sorted
161 fractions. This approach (Figure 2A) enabled us to identify sgRNAs that are significantly enriched in the
162 fraction of the population with highest FSC values. These sgRNAs point to genes or operons necessary to
163 maintain normal cell size.
164

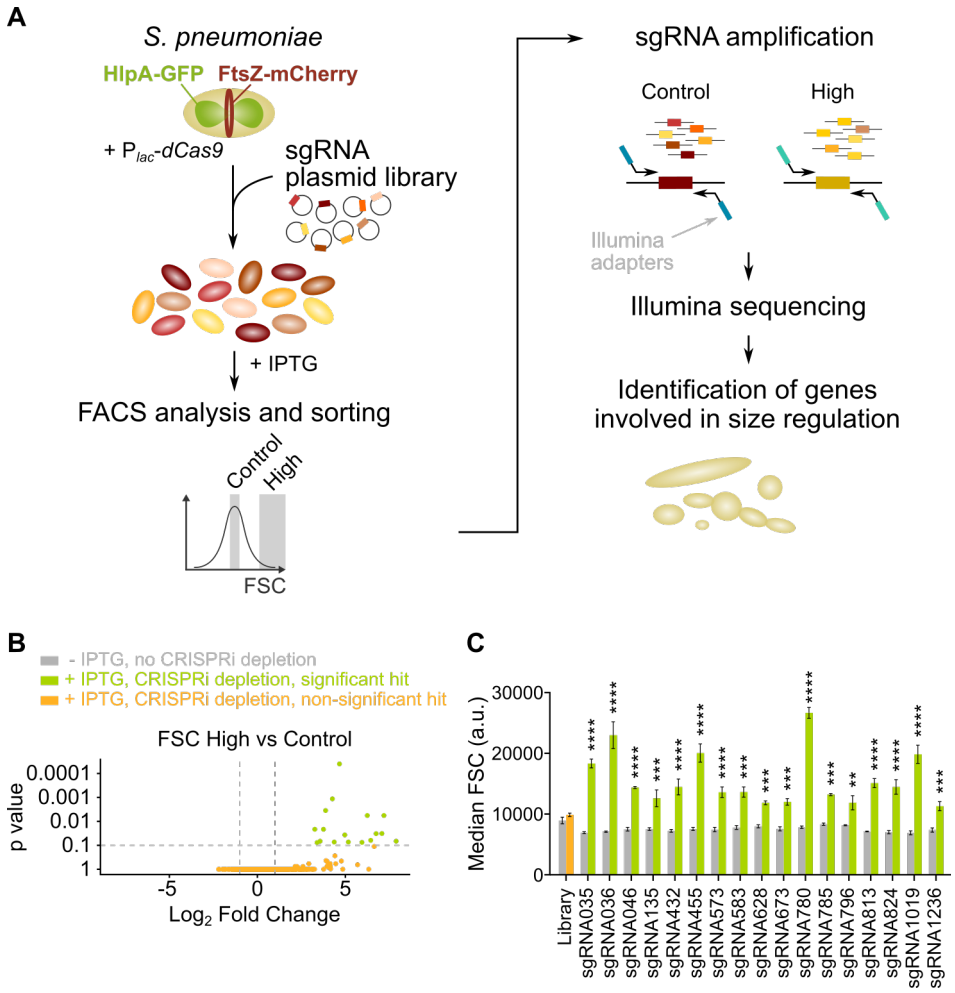

165
166 **Figure 2: sCRilecs-seq identifies operons involved in cell size regulation.** A) A pooled CRISPRi library was constructed in *S.*
167 *pneumoniae* D39V P_{lac}-*dcas9 lacI hlpA-gfp ftsZ-mCherry* (VL3117) by transformation of a plasmid library encoding 1499

168 constitutively-expressed sgRNAs that together target the entire genome. This CRISPRi library was grown in the presence of IPTG
169 for 3.5h to induce expression of dCas9, and cultures were sorted based on forward scatter (FSC) as a proxy for cell size. 10% of
170 the population with the highest FSC values was sorted, as well as the centermost 70% of the population which served as a control.
171 sgRNAs from sorted fractions were amplified by PCR using primers that contain Illumina adapters. Amplified sgRNAs were
172 sequenced and mapped to the *S. pneumoniae* genome. sgRNA read counts were compared between the different sorted fractions
173 to identify gene depletions that lead to increases in cell size. B) A volcano plot shows the statistical significance and enrichment
174 for every sgRNA in the fraction of the population with high FSC values compared to the control with normal FSC values. C)
175 Significant sgRNA hits were validated by studying individual mutants. Flow cytometry measurements of mutants grown with and
176 without IPTG were compared. Note that the entire CRISPRi library was also included in this experiment ('Library') as a control.
177 Data are represented as mean ± SEM, n = 3. ** $p < 0.01$, *** $p < 0.001$, **** $p < 0.0001$, two-sided t-tests with Holm-Sidak
178 correction for multiple comparisons.
179

180 **sCRilecs-seq identifies several targets involved in maintaining proper cell size**

181 Following this strategy, we were able to identify 17 sgRNAs that were significantly enriched in the fraction
182 of the population with high FSC values (Figure 2B, Figure S1D-E and Table S1), indicating that depletion of
183 these sgRNA targets leads to an increase in cell size. The relatively low amount of significant hits isolated
184 here, and the absence of a couple of known cell cycle regulators, such as GpsB[41,42], indicates that false
185 negative results are probably quite common. This is perhaps not surprising given the high amount of
186 variation detected between different repeats (Figure S1D-E). We also note that some knock down mutants
187 that are highly sensitive to physical perturbations might be lost due to the vigorously vortexing of cells
188 prior to FACS. In a next step, we validated whether the 17 significant hits from our sCRilecs-seq screen
189 were correctly identified. The corresponding sgRNAs were individually cloned and transformed to strain
190 D39V P_{lac}-*dcas9 lacI hlpA-gfp ftsZ-mCherry* (VL3117) and their effect was evaluated by flow cytometry. The
191 median FSC value for each depletion was recorded and compared to the median value of the same strain
192 without induction of dCas9. As shown in Figure 2C, all of the significant FSC hits from the sCRilecs-seq
193 screen demonstrated increased FSC levels upon depletion, meaning that no false positives were identified
194 by the cell sorting approach used in our sCRilecs-seq screen and that all selected sgRNAs indeed affect FSC
195 values and therefore likely change cell size.
196

197 The reliability of our screening approach is also reflected by the fact that many of the significant hits are
198 known to be involved in processes that influence cell size and/or morphology (Table S1). For example, 3
199 out of 17 hits are involved in cell division (i.e. *divIB*, *ftsL*, *ylmH*), 1 hit interferes with peptidoglycan
200 synthesis (*murF*) and at least 3 hits target the production of teichoic acids (*licD1*, *tacF*, *tacL*, and the operon
201 containing *tarQ*, *tarP* and *licD3*). These glycopolymers are an important component of the *S. pneumoniae*

202 cell envelope and are necessary to maintain proper cell morphology[21,43,44]. The fact that these hits are
203 picked up by our screen demonstrates that our strategy is capable of extracting biologically relevant
204 information.
205
206 Interestingly, when performing Gene Ontology (GO) enrichment[45-47] to look for biological processes that
207 are found among the hits more often than expected based on random chance, one biological process, i.e.
208 biosynthesis of isoprenoids, was found to be significantly overrepresented (Fold Enrichment = 56, P value
209 = 0.0019). We therefore decided to further focus on isoprenoid biosynthesis and how disturbances in this
210 process lead to changes in *S. pneumoniae* cell size that might be exploited as a novel antimicrobial
211 strategy.
212
213 **Depletion of mevalonate pathway components leads to cell elongation**
214 *S. pneumoniae* synthesizes isoprenoids through the mevalonate pathway[30,48]. This pathway, with
215 mevalonic acid (mevalonate) as intermediate, produces the C5 precursors, isopentenyl diphosphate and
216 dimethylallyl diphosphate (Figure 3A), which can be condensed into large and diverse isoprenoids[30]. In *S.*
217 *pneumoniae*, all proteins involved in the mevalonate pathway are encoded by two different operons[48,49],
218 both of which were identified as hits in our sCRilecs-seq screen. In a first step, we made non-CRISPRi-
219 based deletion/complementation strains for both of these operons. In an *S. pneumoniae* D39V strain that
220 encodes the *hlpA-gfp* and *ftsZ-mCherry* fusion proteins as well as LacI (VL3404), complementation
221 constructs for the mevalonate genes under control of the IPTG-inducible P_{lac} promoter were inserted
222 ectopically into the genome and the native mevalonate genes were deleted (Figure 3B). The resulting two
223 deletion/complementation strains (VL3565 and VL3567) were then used to assess the effect of
224 mevalonate synthesis on cell size and growth.
225
226 Phase contrast microscopy on cells depleted for the mevalonate pathway operons demonstrated large
227 increases in cell length (Figure 3C-D and S2A), confirming the sCRilecs-seq screen. Even though cells also
228 became slightly wider upon mevalonate depletion (Figure 3C), cell length was disproportionally affected.
229 Cells on average attained more than twice their normal length when the mevalonate operons were
230 depleted (Figure 3D and S2A), whereas the mean cell width only increased 1.35x for depletion of operon
231 1 and 1.25x for operon 2. The disproportionately large effect on cell elongation is also demonstrated by
232 significant increases in the length/width ratio (Figure S2A). In addition to cell elongation, depletion of the
233 mevalonate operons led to severe growth defects (Figure 3E). Importantly, the elongated phenotype and

234 observed growth defects could be complemented by ectopic induction of the mevalonate operons with
235 an optimized concentration of IPTG (Figure 3F-G), demonstrating that these phenotypes are not due to
236 polar effects of the mutations. Time lapse microscopy upon depletion of the mevalonate operons
237 confirmed these findings, showing that cells initially continue to grow and elongate before lysis takes place
238 (Figure 3J and Movie S2-3). Of note, these phenotypes were reproducible in deletion/complementation
239 strains that do not carry the *hlpA-gfp* and *ftsZ-mCherry* fusions (VL3708 and VL3709) (Figure S2B-E).
240
241 Although the severe growth defects associated with depletion of the genes involved in mevalonate
242 biosynthesis point to the importance of this pathway for *S. pneumoniae* physiology, cultures were not
243 fully sterilized at late time points and many survivors remained (Figure 3E). To test whether the
244 mevalonate pathway is essential for *S. pneumoniae* viability and that the survival of the depletion strains
245 at late time points is due to leaky expression and/or suppressor mutations, we attempted to delete the
246 mevalonate operons without providing a complementation construct. As expected for essential genes, we
247 were unable to delete these operons. However, when mevalonic acid – an intermediary in the mevalonate
248 pathway (Figure 3A) – was added to the growth medium, we were able to delete operon 1, as was also
249 shown previously in *S. pneumoniae* and *S. aureus*[48,50-52]. As expected based on pathway architecture,
250 deleting operon 2 – which encodes proteins that work downstream of mevalonic acid – remained
251 impossible. We next grew *S. pneumoniae* Δ*operon 1* (VL3702) with different concentrations of mevalonic
252 acid. Cells grew normally and attained normal cell lengths when a high concentration of mevalonic acid
253 was added to the growth medium (Figure 3H-I). However, decreasing the concentration of mevalonic acid
254 led to cell elongation and growth defects that became more pronounced at lower concentrations, thereby
255 phenocopying genetic depletion of operon 1 and 2. In fact, when no mevalonic acid is provided at all,
256 cultures are driven to full extinction (Figure 3I). These results confirm that the mevalonate pathway is
257 essential for *S. pneumoniae* viability and that it is the only pathway through which this bacterium can
258 synthesize isoprenoids[48].
259

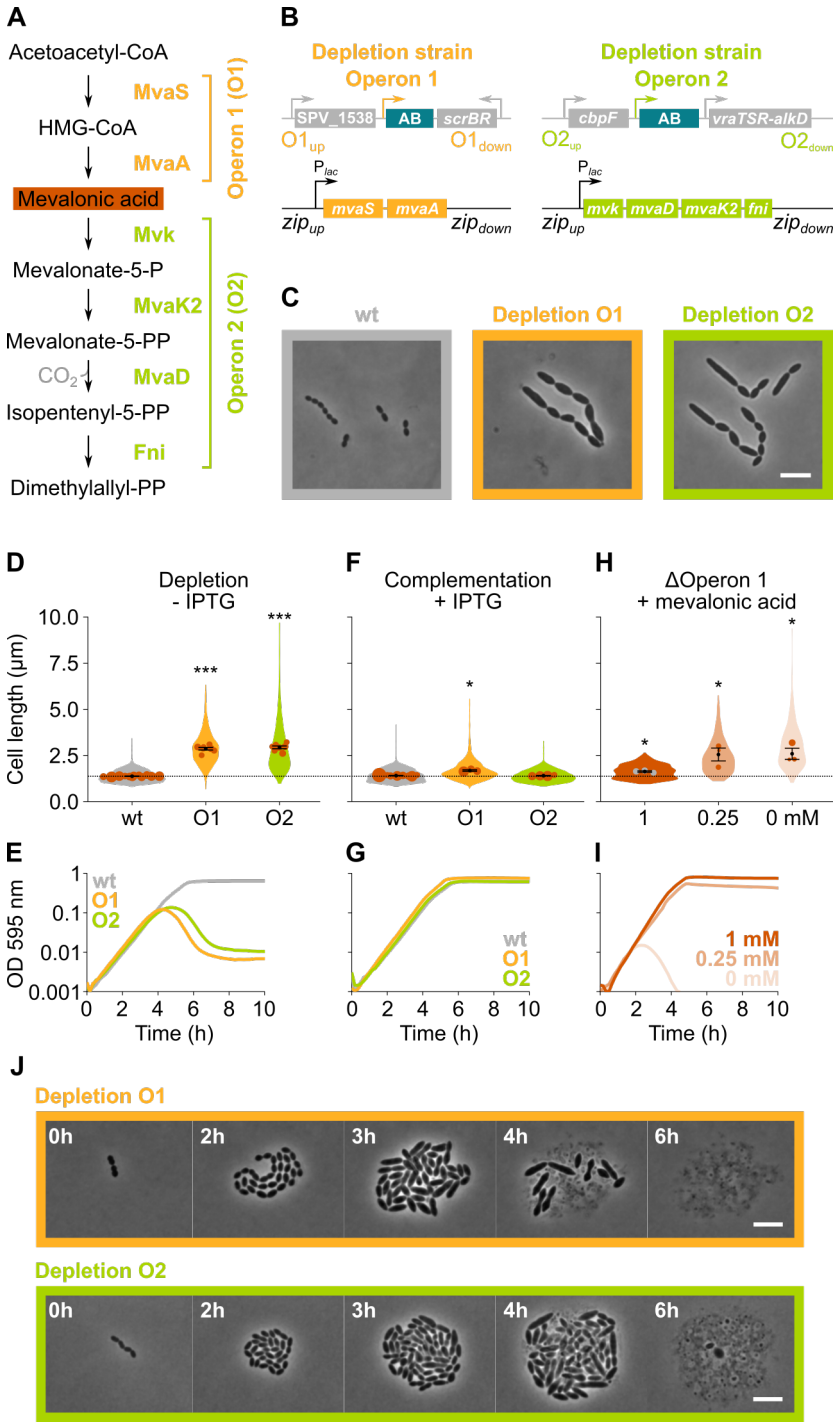

Figure 3: The mevalonate pathway is essential for *S. pneumoniae* and leads to cell elongation upon depletion. A) The mevalonate pathway and its genetic organization in *S. pneumoniae* is depicted. B) A genetic representation of the mevalonate depletion strains is shown. The native mevalonate operons were deleted and replaced by an antibiotic marker (AB) and a complementation construct under control of the P_{lac} promoter was inserted at the *zip* locus[53] in the *S. pneumoniae* genome. C) Phase contrast microscopy images of *S. pneumoniae* wt or upon depletion of one of the mevalonate operons for 4h in VL3565 and VL3567 are shown. Scale bar, 5 µm. D) Quantitative analysis of phase contrast micrographs shows that cell length increased when mevalonate operons were depleted. Data are represented as violin plots with the mean cell length of every biological

268 repeat indicated with orange dots. The size of these dots indicates the number of cells recorded in each repeat, ranging from 100
269 to 2626 cells. Black dots represent the mean ± SEM of all recorded means, n ≥ 3.
270 E) Depletion of mevalonate operons led to a severe growth defect. Data are represented as the mean, n ≥ 3. F) The elongated
271 phenotype upon depletion of mevalonate operons could be complemented by inducing their expression with IPTG. Data are
272 represented as violin plots with the mean cell length of every biological repeat indicated with orange dots. The size of these dots
273 indicates the number of cells recorded in each repeat, ranging from 100 to 2626 cells. Black dots represent the mean ± SEM of all
274 recorded means, n ≥ 3. G) The growth defect associated with depletion of mevalonate operons could be fully complemented by
275 inducing their expression with IPTG. Data are represented as the mean, n ≥ 3. H) A mutant in which the first mevalonate operon
276 was deleted (VL3702, no complementation construct) displayed increased cell length when the concentration of mevalonic acid
277 added to the growth medium was decreased. Data are represented as violin plots with the mean cell length of every biological
278 repeat indicated with orange (or grey) dots. The size of these dots indicates the number of cells recorded in each repeat, ranging
279 from 100 to 2626 cells. Black dots represent the mean ± SEM of all recorded means, n ≥ 3. I) Growing the mutant in which the
280 first mevalonate operon is deleted (no complementation construct) with decreasing concentrations of external mevalonic acid
281 led to an increasing growth defect, resulting in full extinction of the culture when no mevalonic acid was provided. Data are
282 represented as the mean, n ≥ 3. J) Snapshot images of phase contrast time lapse experiments with mutants in which the first or
283 second mevalonate operon was depleted (VL3565 and VL3567) are shown. Strains were grown on agarose pads of C+Y medium
284 without the inducer IPTG. Scale bar, 5 µm. Two-sided Wilcoxon signed rank tests were performed against wt - IPTG as control
285 group (dotted line) and p values were adjusted with an FDR correction; * $p < 0.05$, *** $p < 0.001$.
286

287 **Depletion of mevalonate operons primarily interferes with cell division**

288 We next asked how depletion of mevalonate pathway components results in an elongated phenotype.
289 Microscopic investigation of mevalonate depleted cells showed that these bacteria contain a large
290 number of unconstricted FtsZ rings (Figure 4A-B). High-resolution investigation of this phenotype by
291 Transmission Electron Microscopy (TEM) showed that depletion of the mevalonate operons resulted in
292 an unusually high occurrence of initiated septa that appear to be blocked for further constriction, whereas
293 division septa at all stages of constriction could be found in a wild-type strain (Figure 4C). The inability to
294 constrict and divide could explain the observed filamentation if cell elongation still occurs.
295

296 To investigate if indeed peptidoglycan synthesis for cell elongation remains active upon depletion of the
297 mevalonate operons, we labeled sites of active peptidoglycan synthesis with Fluorescent D-Amino Acids
298 (FDAAs)[54]. In a first pulse, cells were labeled with the green FDAA, sBADA, for 15 min and a second 15 min
299 pulse consisted of the red FDAA, RADA (see Materials and Methods). Fluorescence microscopy showed
300 that peptidoglycan synthesis leads to both cell elongation and division in a wt strain (Figure 4D). Likewise,
301 also the mevalonate depletion strains showed sites of active peptidoglycan synthesis, indicating that not
302 all cell wall production is halted. However, in this case, we almost exclusively detected peptidoglycan

303 synthesis directed at cell elongation since almost no constricted FDAA-labeled sites were found (Figure
304 4D-E).. Additionally, it is clear that even though peptidoglycan synthesis continues upon mevalonate
305 depletion, this process is slowed down since FDAA intensity is decreased under these conditions,
306 indicating that less peptidoglycan is being produced (Figure 4D). Quantification of the intensity of the
307 sBADA signal indeed confirmed that the incorporation of the label is strongly decreased upon mevalonate
308 depletion (Figure 4F). The same quantification was not done for the RADA label since the relatively high
309 aspecific background fluorescence interfered strongly with this analysis.
310
311 Taken together, these results strongly indicate that mevalonate depletion leads to filamentation because
312 cell division is blocked while peptidoglycan synthesis for cell elongation can still occur, albeit at a lower
313 rate. However, elongation does not continue indefinitely and cells eventually lyse (Figure 3J and Movie
314 S3-4). Since lysis usually occurs through weakening of the peptidoglycan cell wall[56], we hypothesize that
315 extended depletion of mevalonate operons eventually affects the integrity and/or rigidity of the
316 peptidoglycan mesh, leading to cell lysis. However, considering the initial phenotypes found, we conclude
317 that the primary effect of mevalonate depletion is a block in constriction necessary for cell division.
318

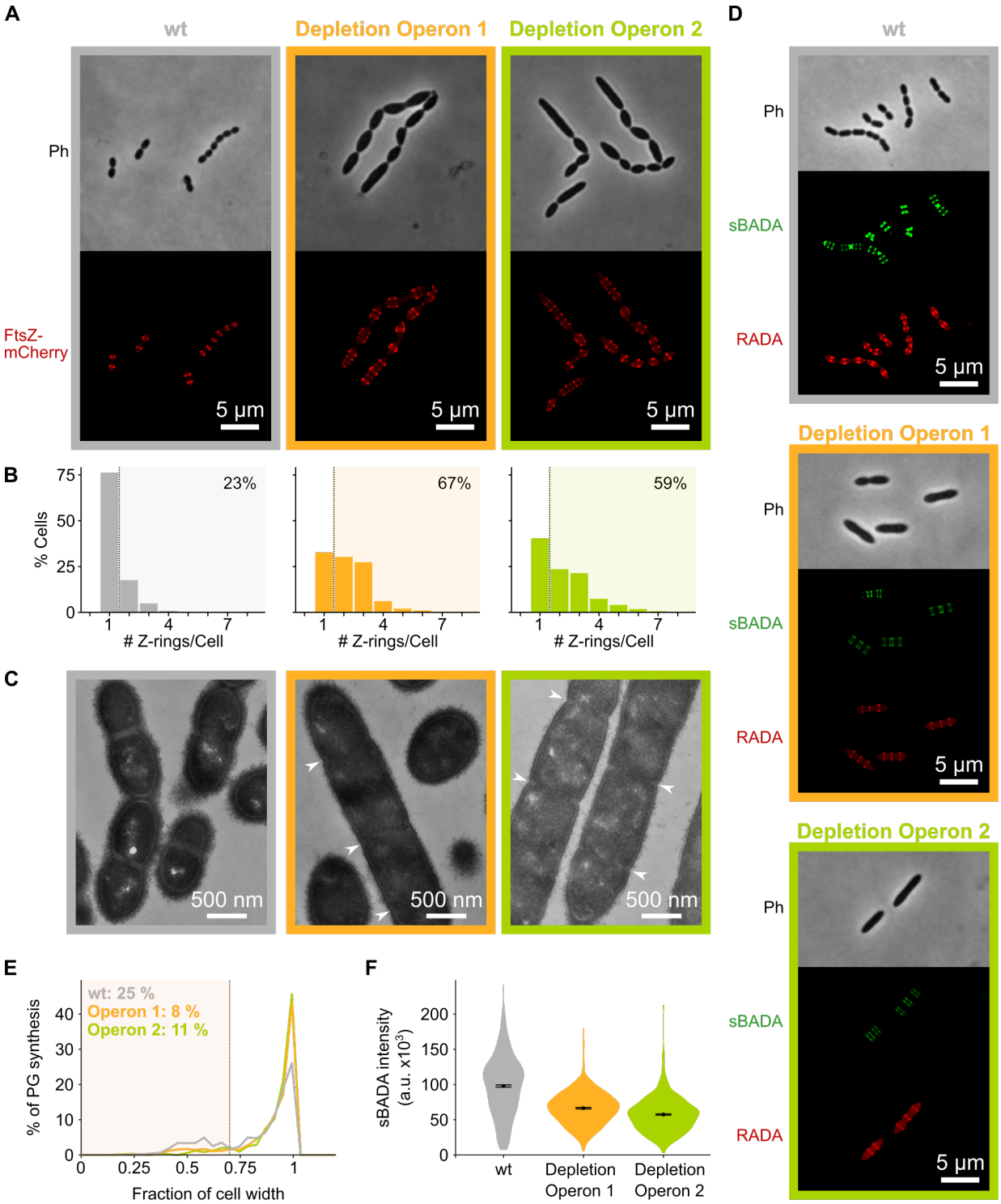

Figure 4: Depletion of mevalonate operons prevents cell division. A) While *S. pneumoniae* wt cells typically contain one FtsZ ring at the cell center, depletion of either one of the mevalonate operons led to strongly elongated cells with multiple unconstricted FtsZ rings. Images were obtained using strains VL3404, VL3565 and VL3567 that encode the *ftsZ-mCherry* fusion. B) Quantitative analysis of microscopy pictures was used to determine the number of Z-rings per cell. Pictures from at least 6 independent repeats were analyzed, each including over 100 cells. C) Transmission Electron Microscopy (TEM) images show that elongated cells

contained many initiated septa that appear to be blocked in further progression of constriction (white arrow heads). Images were obtained using strains VL333, VL3708 and VL3709 that do not encode fluorescent fusion proteins. D) Pulse labeling *S. pneumoniae* with the green FDAA, sBADA, and 15 min later with the red RADA shows sites of active peptidoglycan synthesis involved in either elongation or constriction. Images were obtained using strains VL333, VL3708 and VL3709 that do not encode fluorescent fusion proteins. E-F) Quantitative image analysis of sites of active peptidoglycan synthesis labeled with FDAAs shows that depletion of mevalonate operons eliminated septal peptidoglycan synthesis since virtually no narrow sBADA or RADA bands can be found (E) and that the intensity of FDAA labeling decreased upon mevalonate depletion, indicating that peripheral peptidoglycan synthesis was slowed down (F). Number of sBADA bands analyzed for each condition > 400.

Depletion of mevalonate operons prevents cell division by limiting the export of peptidoglycan precursors

The mevalonate pathway provides the precursor for the production of all isoprenoids in *S. pneumoniae*[30,48]. Thus, a shortage in the production of any of these isoprenoids could underlie the phenotypic effects of perturbed mevalonate production. However, given the nature of the observed phenotype, we thought it most likely that a shortage in the production of undecaprenyl phosphate (Und-P) would be responsible for the observed effects. Und-P is a C55 isoprenoid that acts as the lipid carrier for transport of cell envelope precursors from the cytoplasm to the extracellular environment[32]. Und-P is produced by the dephosphorylation of undecaprenyl pyrophosphate (Und-PP), which is in turn synthesized by UppS (undecaprenyl pyrophosphate synthase) by the addition of 8 isopentenyl units to the C15 isoprenoid farnesyl-PP[30,32] (Figure 5A). To test whether the observed effects of mevalonate depletion are indeed caused by a deficiency of Und-P, we constructed a *uppS* deletion/complementation strain (VL3584, Figure 5B). When this strain was grown in absence of *uppS* expression, cells were elongated and growth was reduced (Figure 5C-D), thereby phenocopying mevalonate mutants. In addition, UppS depleted cells contained multiple unconstricted Z-rings and initiated septa that failed to constrict further, even though peptidoglycan synthesis still occurred as demonstrated by TEM and fluorescence microscopy (Figure 5D-F). Note that *uppS* was not identified by our sCRilecs-seq screen, likely because it is in an operon with several other essential genes not directly involved in cell division, such as *cdsA* and *proS*[49]. We thus conclude that the negative effects caused by depletion of the mevalonate operons can be explained by insufficient production of Und-PP and subsequently Und-P.

The isoprenoid Und-P carries precursors of the capsule, teichoic acids and peptidoglycan across the membrane[32]. The observed phenotype of mevalonate and *uppS* mutants could therefore be caused by a shortage in either one or a combination of these components. To test which of these pathways contribute

358 to the observed phenotypes upon mevalonate depletion, we tested each of them individually. First, we
359 deleted the *cps* operon responsible for capsule synthesis in our D39V strain[57]. As shown in Figure S3A-B,
360 *cps* mutant cells were not elongated nor was growth rate affected, as also shown before[58], demonstrating
361 that a shortage of capsule synthesis does not contribute to the mevalonate depletion phenotype. Next,
362 we focused on the possible contribution of both teichoic acid and peptidoglycan synthesis by depleting
363 the enzymes responsible for coupling the final cytoplasmic precursors to Und-P before transport to the
364 outside of the cell. For peptidoglycan, it is known that the MurNAc-pentapeptide moiety that is produced
365 in the cytoplasm is coupled to Und-P by MraY[32]. Based on sequence similarity, bioinformatic analysis
366 indicated that the enzyme that does the same for teichoic acid precursors in *S. pneumoniae* is SPV_1620[59].
367 Deletion/complementation strains for these genes were created and the effect of depletion of either
368 MraY or SPV_1620 was assessed (strain VL3585 and VL3586, respectively). Surprisingly, depletion of
369 neither MraY nor SPV_1620 produced cell morphologies that resembled mevalonate operon depletions
370 at the time we usually assess them (Figure 5G-H, time point 4h). However, since at this time cells were
371 severely malformed and many had already lysed, we decided to follow these depletions through time and
372 also record morphologies at earlier time points. Figure 5G shows the progression of these depletions in
373 terms of average cell length, while Figure 5H shows representative morphologies. From this analysis it
374 became clear that, although depletion of both MraY and SPV_1620 led to increased cell length, the
375 phenotype obtained upon SPV_1620 depletion differed profoundly from the phenotypes found when
376 depleting mevalonate operons. Depletion of MraY, on the other hand, was highly similar to the
377 mevalonate phenotype at early time points. We thus conclude that a deficiency in the export of
378 peptidoglycan precursors is mainly responsible for the elongated phenotype that is observed when
379 components of the mevalonate pathway are depleted. Since we previously showed that this elongated
380 phenotype is caused by continued peptidoglycan synthesis in the absence of cell constriction, it appears
381 as though a certain threshold level of peptidoglycan precursors is needed for cells to divide. Cell
382 elongation, on the other hand, can proceed with a lower amount of peptidoglycan precursors indicating
383 switch-like behavior between elongation and constriction[43].
384

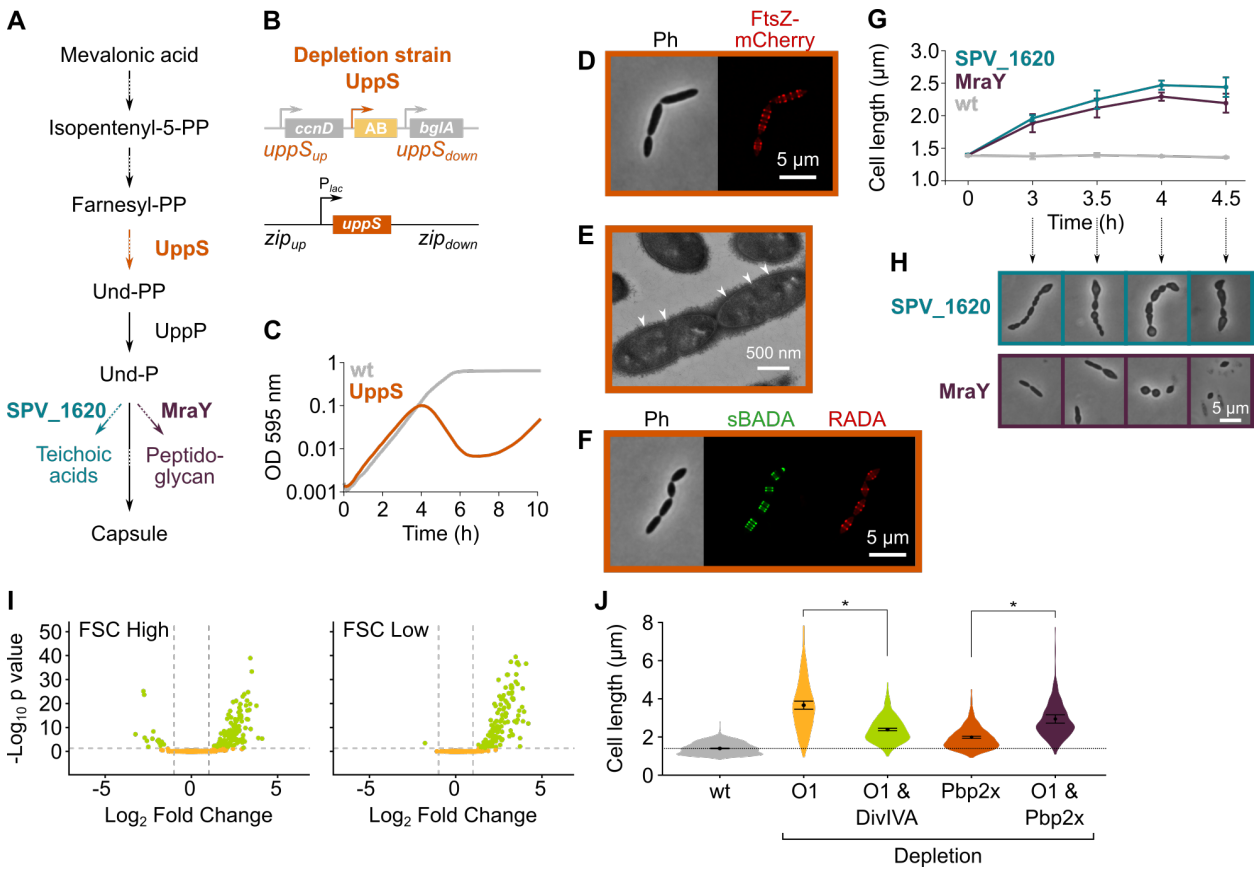

Figure 5: Depletion of the mevalonate pathway likely prevents cell division by limiting the export of peptidoglycan precursors which preferentially inhibits cell division. A) After conversion of mevalonic acid into the basic isoprenoid building block isopentenyl-5-PP in the mevalonate pathway, this building block is condensed into the C15 molecule Farnesyl-PP. Farnesyl-PP can be used by UppS for the production of undecaprenyl pyrophosphate (Und-PP), which after dephosphorylation to Und-P by UppP acts as the lipid carrier for the transport of precursors of peptidoglycan, the capsule and teichoic acids across the cell membrane. B) A genetic overview of the UppS depletion strains is shown. The native *uppS* gene was replaced by an antibiotic marker (AB) and a complementation construct under control of the P_{lac} promoter was inserted at the *zip* locus in the *S. pneumoniae* genome. C) Depletion of UppS in VL3584 caused a growth defect similar to depletion of the mevalonate operons. We confirmed that the growth observed after an initial phase of lysis was due to suppressor mutants that are no longer sensitive to UppS depletion (Figure S3C). Data are represented as averages, n ≥ 3. D) Like depletion of the mevalonate operons, depletion of UppS caused an elongated phenotype where cells contained multiple unconstricted FtsZ rings. Images were obtained using strain VL3585 which encodes *ftsZ-mCherry*. E) Transmission Electron Microscopy (TEM) images show that cells elongated due to UppS depletion contained many initiated septa that appeared to be blocked in further progression of constriction (white arrow heads). Images were obtained using strain VL3710 that does not encode fluorescent fusion proteins. F) Pulse labeling *S. pneumoniae* depleted for UppS with the green FDAA, sBADA, and subsequently with the red RADA dye showed sites of active peptidoglycan synthesis, which are in this case all directed at cell elongation. Images were obtained using strain VL3710 that does not encode fluorescent fusion proteins. G) The effect of the depletion of MraY and SPV_1620 on cell length was followed through time using quantitative image analysis. For each biological repeat (n ≥ 3), more than 50 cells were used to calculate the average cell length. Data are represented as the mean ± SEM of these averages. H) Representative morphologies of VL3585 and VL3586 corresponding to the

405 analysis from panel G are shown. I) A pooled CRISPRi library was constructed in VL3834 (*S. pneumoniae* D39V P_{lac}-*dCas9* Δ*mvaA*-
406 *mvaS*). This CRISPRi library was grown in the presence of the dCas9 inducer, IPTG, and limiting amounts of mevalonic acid (100
407 µM). Cultures were sorted based on cell size (FSC); 10% of the population with the highest and lowest values were sorted, as well
408 as the centermost 70% of the population which served as a control. sgRNAs from the sorted fractions were sequenced and read
409 counts were compared to identify gene depletions that led to changes in cell size. Volcano plots show the statistical significance
410 and enrichment for every sgRNA in the fraction with high FSC values (FSC High) and low FSC values (FSC Low) compared to the
411 control. J) Quantitative analysis of microscopy images shows the changes in cell length upon single or double depletions of the
412 first mevalonate operon (O1, *mvaS*-*mvaA*), DivIVA or Pbp2x. Data are represented as violin plots with the mean ± SEM indicated,
413 n ≥ 3, with each repeat containing > 90 cells except for the double O1 Pbp2x depletion where not enough surviving cells could be
414 visualized and the threshold was put at 10 cells. Two-sided Wilcoxon signed rank tests were performed and p values were adjusted
415 with an FDR correction; * $p < 0.05$.
416

417 **A sCRilecs-seq screen on mevalonate depleted cells to study the underlying genetic network**

418 To identify pathways and genes that are particularly sensitive to reduced mevalonate levels, and to obtain
419 clues on why a lowered concentration of extracellular peptidoglycan precursors would allow elongation
420 but not division, we performed a second sCRilecs-seq screen based on cell size (FSC) in a genetic
421 background in which the first mevalonate operon was deleted (VL3834: D39V P_{lac}-*dcas9 lacI* Δ*mvaS*-
422 *mvaA*). This way, we could look for gene depletions that aggravate the observed phenotype, i.e. make
423 cells even longer, and depletions that compensate for the mevalonate-dependent cell elongation. During
424 construction of this CRISPRi library and prior to selection, cultures were grown in the presence of a high
425 concentration of mevalonic acid (1 mM) which ensures wild-type growth and normal cell size even though
426 the first mevalonate operon is deleted (see Figure 3H-I). After construction of the pooled CRISPRi library,
427 cultures were grown with limiting amounts of external mevalonic acid (100 µm) to trigger the elongated
428 phenotype caused by mevalonate deficiency (Figure S4A). Simultaneously, dCas9 expression was induced
429 by the addition of 1 mM IPTG for 3.5h. 10% of the population with the highest and lowest FSC values were
430 sorted by FACS and the centermost 70% of the population was collected to serve as a control. Comparing
431 sgRNA read counts from the collected fractions led to the identification of many significantly enriched
432 targets in the populations with the highest and lowest FSC values (Figure 5I, Figure S4B and Table S2).
433

434 GO enrichment analysis identified cell division and closely related GO categories as significantly
435 overrepresented in elongated cells (Table S3). This suggests that depleting genes involved in cell division
436 will lead to additional cell elongation upon mevalonate depletion. On the other hand, sgRNAs that are
437 enriched in the small fraction of the population are often involved in protein expression (transcription,
438 translation, ribosome assembly, etc.) or energy metabolism. Halting or interfering with protein expression

439 or energy production therefore appears to reduce cell elongation caused by mevalonate deficiency. The
440 results of these high-level analyses are clear; directly interfering with cell division reinforces the division
441 block imposed by mevalonate depletion and inhibiting protein expression or energy production, both of
442 which are necessary for growth in general, prevents cell elongation.
443
444 Additionally, when looking at individual genes and operons found among the significantly enriched hits,
445 some interesting patterns emerge. For example, the sgRNA targeting *divIVA* was strongly depleted from
446 the large fraction of the population and also highly enriched in the small fraction, indicating that the
447 depletion of DivIVA hampers cell elongation upon mevalonate depletion. DivIVA activity was previously
448 shown to be necessary for cell elongation and DivIVA is known to be phosphorylated by the
449 serine/threonine kinase StkP that is thought to constitute a molecular switch that governs elongation and
450 division[43,60-63]. Indeed, we confirmed that a double depletion of the first mevalonate operon and DivIVA
451 leads to reduced cell lengths in comparison to the depletion of mevalonate alone (Figure 5J), indicating
452 that also upon mevalonate depletion DivIVA activity assists cell elongation. However, cells depleted for
453 both mevalonate and DivIVA are still larger than wild-type cells, indicating that a limited amount of
454 elongation still occurs. Elongation enforced by mevalonate depletion is therefore not fully dependent on
455 DivIVA activity. Additionally, CRISPRi depletion of the SEDS proteins FtsW and RodA had opposite effects
456 on cell size in our screen, with FtsW depletion leading to increased cell sizes while RodA depletion causing
457 decreases in cell size (Table S2). These proteins are thought to be the primary transglycosylases
458 responsible for peptidoglycan polymerization during cell division and cell elongation, respectively[64-68].
459 Moreover, CRISPRi depletion of Pbp2b, the transpeptidase that works in conjunction with RodA to
460 perform peripheral peptidoglycan synthesis[43,67,69], showed up in the shorter cell fraction (Table S2). These
461 results are in line with the hypothesis that cell elongation in mevalonate depleted cells is caused by
462 ongoing peripheral peptidoglycan synthesis while septal synthesis is inhibited. If this is true, then
463 depletion of Pbp2x, the essential pneumococcal PBP required for cell division and the prime target of the
464 penicillins including amoxicillin[70], should show a synthetic effect upon mevalonate depletion. As *pbp2x* is
465 located in an operon together with *mraY*, this could not be directly assessed in the sCRilecs-seq screen.
466 Therefore, we constructed a clean *pbp2x* depletion strain. As shown in Figure 5J, depletion of Pbp2x
467 indeed led to an increase in cell length, as reported before[34], and this phenotype was augmented under
468 low mevalonate levels.
469

470 **The mevalonate pathway as druggable target in *S. pneumoniae***

471 Our results so far demonstrate that depletion of the mevalonate pathway leads to cell elongation and
472 these morphological effects can be enhanced by targeting other cell division pathways. Since amoxicillin
473 also causes elongation in *S. pneumoniae*, we set out to design a combination treatment strategy using
474 amoxicillin and exploiting the mevalonate depletion phenotype characterized here. In a first step, we
475 confirmed that the antibacterial effect of amoxicillin – but not that of the fluoroquinolone ciprofloxacin –
476 is increased upon mevalonate depletion, since amoxicillin could inhibit growth already at sub-MIC
477 concentrations when mevalonate became limiting (Figure S5A-B). These results demonstrate that, in
478 principle, it is possible to design a treatment strategy in which amoxicillin is potentiated by targeting the
479 mevalonate pathway.

480

481 In a second step, we looked for chemical compounds that could block either the mevalonate pathway or
482 the downstream production of Und-P. Three compounds were selected; simvastatin and farnesol are
483 expected to block the HMG-CoA reductase MvaA that catalyzes one of the first steps of the mevalonate
484 pathway[71-73], while clomiphene was shown to inhibit UppS in *S. aureus*[33]. To confirm the specificity of
485 these compounds for the mevalonate pathway or downstream production of Und-P, we first tested
486 whether they could induce the expected cell elongation in *S. pneumoniae*. Since only the addition of
487 clomiphene resulted in filamentation under our conditions (Figure 6A), we selected this compound for
488 further testing. Indeed, time lapse analysis showed considerable cell elongation in the presence of
489 clomiphene, albeit less than upon depletion of the mevalonate operons potentially due to the lag in severe
490 effects upon gradual genetic depletion (Figure 6B and Movie S5). Additionally, clomiphene most likely
491 targets the production of Und-P, since sub-MIC concentrations of clomiphene led to severe growth defects
492 in cultures that were slightly depleted for mevalonate (Figure S5C).

493

494 We next combined clomiphene with either amoxicillin or ciprofloxacin at several different concentrations
495 and monitored the growth of an *S. pneumoniae* D39V wild-type strain by measuring OD. The success of
496 growth was quantified by calculating the area under the curve for a growth period of 10 hours. As can be
497 seen in Figure 6C, clomiphene did not affect the efficacy of ciprofloxacin. However, for amoxicillin,
498 potentiation by clomiphene was observed (Figure 6D). This is consistent with time lapse analyses that
499 show that survival of *S. pneumoniae* was much more affected when both compounds were combined
500 (Figure 6E and Movie S6). Indeed, in the presence of clomiphene, the concentration of amoxicillin
501 necessary to block pneumococcal growth decreased by a factor 2 to 8 (Table 1).

502

503 **Resensitizing antibiotic-resistant *S. pneumoniae* strains using clomiphene**

504 We next tested whether the potentiation by clomiphene is also present in clinically-relevant amoxicillin-
505 resistant *S. pneumoniae*. We therefore assessed the growth of a panel of resistant strains in the presence
506 of different concentrations of amoxicillin and clomiphene. The strains we tested are clinical isolates of
507 strains 19F, Spain-23F and 11A[5,74]. Results are presented in Figure 6F-H and Table 1 and show that
508 clomiphene potentiated the antimicrobial activity of amoxicillin also against clinical resistant strains.
509 Moreover, the potentiation was even stronger in these resistant genetic backgrounds. Indeed, the
510 concentration of amoxicillin necessary to block growth of these resistant strains decreased by a factor 16
511 to 64 in the presence of 8 µg/ml of clomiphene (Table 1), thereby reducing resistance below the EUCAST
512 clinical breakpoint for sensitivity (0.5 µg/ml)[75]. Our rationally designed combination treatment strategy
513 can thus resensitize amoxicillin-resistant *S. pneumoniae* strains so that they once again become fully
514 susceptible to amoxicillin *in vitro*. This treatment strategy could therefore prove useful in the fight against
515 amoxicillin-resistant *S. pneumoniae* infections.

516

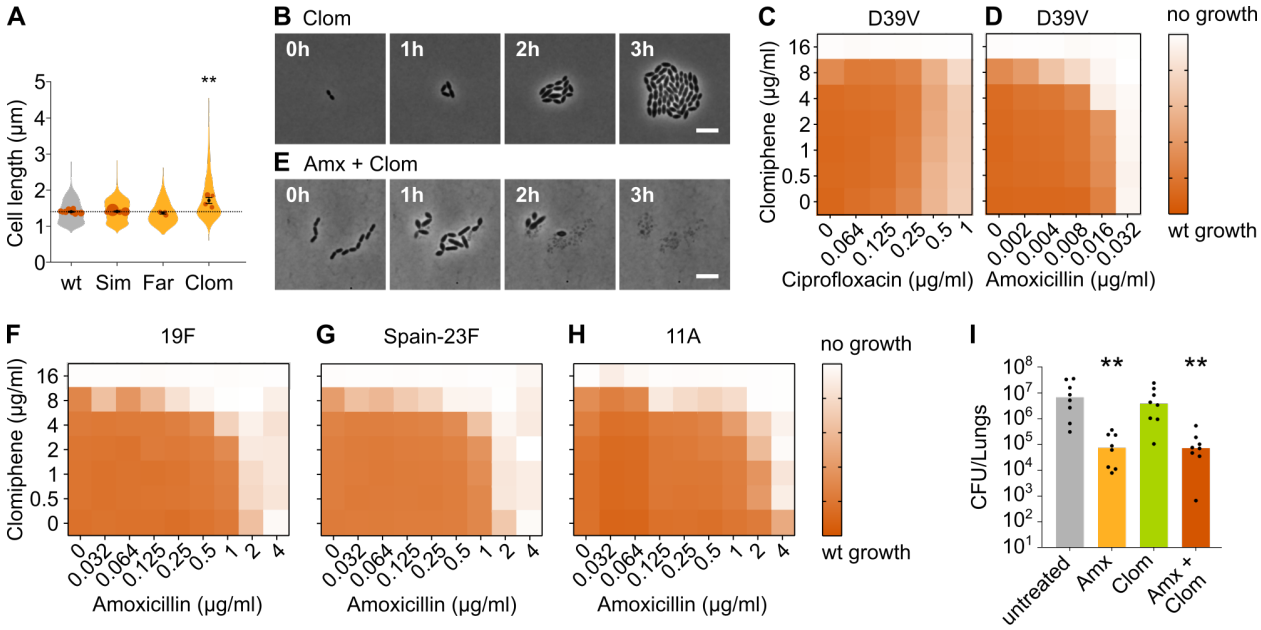

517

518 **Figure 6: Clomiphene, an inhibitor of Und-P production, potentiates amoxicillin.** A) The effect of several potential inhibitors of
519 Und-P production on the cell length of *S. pneumoniae* D39V (VL333) was tested (Sim 4 µg/ml, Far 4 µg/ml, Clom 8 µg/ml).
520 Quantitative analysis of microscopy images shows that cell length increased upon treatment with clomiphene. Data are
521 represented as violin plots with the mean cell length of every biological repeat indicated with orange dots. The size of these dots
522 indicates the number of cells recorded in each repeat, ranging from 177 to 6464 cells. Black dots represent the mean ± SEM of all
523 recorded means, n ≥ 3. Two-sided Wilcoxon signed rank tests were performed against wt without treatment as control group

524 (dotted line) and p values were adjusted with an FDR correction; ** $p < 0.01$. B) Snapshot images of phase contrast time lapse
525 microscopy of *S. pneumoniae* D39V (VL333) in the presence of clomiphene (8 µg/ml). Scale bar, 5 µm. C-D) OD_{595nm} growth curves
526 were constructed for *S. pneumoniae* D39V (VL333) in the presence of different concentrations of clomiphene and ciprofloxacin
527 (C) or amoxicillin (D). Heatmaps of the area under the resulting growth curves are shown. Number of biological repeats for all
528 experiments, $n \geq 3$. E) Snapshot images of phase contrast time lapse microscopy of *S. pneumoniae* D39V (VL333) in the presence
529 of clomiphene (8 µg/ml) and amoxicillin (0.016 µg/ml). Scale bar, 5 µm. F-H) OD_{595nm} growth curves were constructed for *S.*
530 *pneumoniae* 19F (F), Spain-23F (G) and 11A (H) in the presence of different concentrations of clomiphene and amoxicillin.
531 Heatmaps of the area under the resulting growth curves are shown. Number of biological repeats for all experiments, $n \geq 3$. I)
532 The effect of the combination treatment with amoxicillin and clomiphene was tested *in vivo* using a pneumonia superinfection
533 model with a clinical isolate of *S. pneumoniae* serotype 19F. Mice (n=8 per group) were infected intranasally first with H3N2 virus
534 and then 7 days later with pneumococcus 19F. Mice were treated at 8 h and 12h with clomiphene, amoxicillin, combination of
535 both, or left untreated. Lungs were collected 24 h post-infection to measure the bacterial load. CFU counts for individual mice
536 are shown, and the bars represent the median value. The data were compared in a Kruskall-Wallis test (One-Way ANOVA), ** p
537 < 0.01. Wt, wildtype; Sim, simvastatin; Far, farnesol; Clom, clomiphene; Amx, amoxicillin.
538
539 **Table 1: MIC values for amoxicillin/clomiphene and ciprofloxacin/clomiphene drug combinations (µg/ml).**

	Clomiphene		
	0 µg/ml	4 µg/ml	8 µg/ml
S. pneumoniae D39V			
Ciprofloxacin	1	1	1
Amoxicillin	0.032	0.016	0.004
S. pneumoniae 19F			
Amoxicillin	2	1	0.125
S. pneumoniae Spain-23F			
Amoxicillin	2	1	0.032
S. pneumoniae 11A			
Amoxicillin	4	2	0.125

540
541
542 We next tested whether this treatment strategy would prove useful in an *in vivo* setting, using a murine
543 pneumonia disease model (see Materials and Methods)[76]. Mice were infected on day 1 with influenza A
544 virus and superinfected on day 7 with *S. pneumoniae* 19F. Animals were treated with 5 mg of clomiphene
545 and/or 1 mg of amoxicillin at 8 and 12 hours post-pneumococcal infection, respectively. Twenty-four
546 hours post infection, the bacterial load in the lung was determined. Whereas treatment with amoxicillin
547 alone significantly lowered bacterial counts, administering only clomiphene did not influence the bacterial
548 load (Figure 6I). Treating mice with both clomiphene and amoxicillin did not show a stronger effect than
549 treatment with amoxicillin alone, meaning that the potentiation of amoxicillin we observed *in vitro* could

550 not be detected *in vivo* (Figure 6I). The same was true for CFU counts in the spleen (Figure S5D). To figure
551 out why our combination treatment strategy was not effective *in vivo*, we tried to estimate the active
552 concentration of clomiphene in the lung. Our *in vitro* tests showed that potentiation occurs at
553 concentrations of clomiphene of 4 µg/ml and higher, but these concentrations might not be achieved *in*
554 *vivo*. We therefore tested the growth of *S. pneumoniae* D39V *in vitro* in the presence of bronchoalveolar
555 lavage (BAL) fluid collected from mice treated with clomiphene. This experiment indicated that the active
556 concentration of clomiphene in the lung was lower than 4 µg/ml, which could explain the absence of
557 amoxicillin potentiation (Figure S5E).
558
559 **Discussion**
560 Here, we rationally designed a combination treatment strategy that resensitizes resistant *S. pneumoniae*
561 strains towards clinically relevant concentrations of amoxicillin, one of the most widely used antibiotics
562 to fight this human opportunistic pathogen[15-17]. By combining amoxicillin with the FDA-approved fertility
563 drug clomiphene[77-79], we were able to reduce amoxicillin MIC values of resistant strains 16 to 64-fold *in*
564 *vitro*, thereby decreasing them below the EUCAST clinical breakpoint for sensitivity.
565
566 ***sCRilecs-seq identifies several targets that regulate S. pneumoniae cell size***
567 This combination treatment strategy was based on the results of the sCRilecs-seq screen developed here.
568 sCRilecs-seq is a high-throughput single-cell-based screening approach that relies on genome-wide
569 CRISPRi depletion combined with sorting of cells that display a phenotype of interest. We here screened
570 for CRISPRi gene depletions that, like amoxicillin treatment, result in cell elongation. The rationale behind
571 this strategy is that synergy is most often detected between compounds that target the same process[36].
572 Although we used the sCRilecs-seq method to screen for increases in cell size, this approach could easily
573 be adapted to asses any phenotype of interest that can be measured by flow cytometry. In contrast to
574 'classic' CRISPRi-seq screens[22-27], our approach is therefore not limited to measuring changes in fitness but
575 can be used to evaluate a wide array of different phenotypes. Moreover, we show that sCRilecs-seq hits
576 are highly reliable since no false positives were detected in our screen. Interestingly, significant hits
577 include a number of genes of unknown function that we can now implicate in the maintenance of proper
578 cell size. Our sCRilecs-seq approach is thus able to uncover novel gene functions and can help to expand
579 knowledge on any process of interest that can be evaluated using flow cytometry. On the other hand,
580 several genes known to be involved in cell size regulation were not identified as significant hits. Such false
581 negatives could be caused by a variety of reasons. For example, simultaneous repression of all genes in

582 an operon can obscure phenotypes expected upon repression of individual genes. Additionally, depletion
583 of genes that lead to cell lysis cause the corresponding sgRNAs to disappear from the library thereby
584 complicating their identification as hits. Depletion strains sensitive to mechanical vortexing might also be
585 missed. Finally, the high variation detected across different repeats led to large P-values for many targets,
586 even when they were very highly enriched. This high variation thereby limits the number of significant
587 hits that could be detected.
588
589 ***Depletion of mevalonate pathway genes leads to cell elongation through inhibition of cell division***
590 The sCRilecs-seq screen performed here revealed an important role for the mevalonate pathway in
591 maintaining proper cell size. Indeed, depletion of the genes involved in this pathway led to a very strong
592 increase in cell length. Results obtained here strongly indicate that this cell elongation is due to a
593 deficiency in the production of Und-P, the lipid carrier that translocates all different cell envelope
594 precursors across the cell membrane[32], and subsequent limitation of the amount of peptidoglycan
595 building blocks that is being transported. The limiting amount of peptidoglycan precursors available for
596 cell wall synthesis led to an interesting phenotype. Whereas the peptidoglycan synthesis rate in general
597 decreased, peptidoglycan synthesis for cell elongation continued long after constriction for cell division
598 was inhibited. This observation points towards a difference in affinity and/or regulation of elongation and
599 constriction, where it appears that a certain threshold concentration of peptidoglycan precursors needs
600 to be exceeded in order for cell division to take place. Several potential explanations for this observation
601 can be put forward. First, it is possible that peptidoglycan synthesis enzymes dedicated to cell division
602 have a lower affinity for peptidoglycan precursors than their counterparts that function in cell elongation.
603 When cell wall precursors become limiting, the enzymes involved in septal ring closure would be
604 outcompeted and cell division would cease while elongation still occurs. On the other hand, it has
605 previously been suggested that a more complex regulatory mechanism decides whether cells elongate or
606 divide. The serine/threonine kinase StkP and its cognate phosphatase PhpP were suggested to constitute
607 a molecular switch that coordinates septal and peripheral peptidoglycan synthesis through
608 phosphorylation and dephosphorylation of its targets[43,60-62]. This switch is regulated by GpsB, which is
609 necessary for maximal phosphorylation in *S. pneumoniae* and is essential for viability[41,42,80]. Interestingly,
610 depletion of GpsB leads to an elongated phenotype with unconstricted cell division sites[41,42] that is highly
611 reminiscent of the mevalonate depletion phenotype, hinting at possible crosstalk between both
612 pathways. Results presented here indicate that the decision between elongation or division depends on
613 the amount of peptidoglycan precursors that is exported. Potentially, the concentration of precursor

614 molecules influences the activity of GpsB, StkP and/or PhpP and thereby activates this switch. Since StkP
615 contains PASTA domains that are known to bind peptidoglycan precursors[43,60,61,81], it has been suggested
616 that its activity is indeed regulated in response to the concentration of peptidoglycan building blocks
617 present[43,60,61]. However, it was previously shown that even though PASTA domains are necessary for StkP
618 activation, peptidoglycan binding is not required[81], arguing against StkP being a sensor for peptidoglycan
619 precursor levels. Moreover, the depletion of DivIVA upon reduced mevalonate conditions still allowed a
620 modest amount of cell elongation to occur. Since DivIVA is thought to be an important part of the
621 molecular switch between elongation and division instigated by StkP[41,62,63], it appears as though
622 elongation upon mevalonate depletion is at least partially independent of this molecular switch.
623 Therefore, further research will be necessary to determine why elongation is favored over division when
624 peptidoglycan precursors become limiting. Finally, it is possible that depletion of mevalonate pathway
625 components and probable subsequent peptidoglycan precursor shortage induces transcriptional or post-
626 transcriptional regulatory pathways that differentially affect the activity of protein complexes involved
627 cell elongation and division, thereby leading to filamentation.
628
629 ***Inhibition of Und-P synthesis by clomiphene resensitizes resistant S. pneumoniae to amoxicillin***
630 We successfully exploited the knowledge gained on the mevalonate depletion phenotype to fight
631 amoxicillin-resistant *S. pneumoniae* strains. To do so, we confirmed that clomiphene, a compound known
632 to block Und-P production in *S. aureus* and potentiate β-lactam antibiotics, even towards MRSA[33], elicits
633 the elongated mevalonate depletion phenotype in *S. pneumoniae* and therefore most likely also inhibits
634 Und-P production in this bacterium. We next combined clomiphene with the β-lactam antibiotic
635 amoxicillin that preferentially interferes with cell division[69,70]. Results demonstrated that clomiphene can
636 enhance the antimicrobial effect of amoxicillin in a D39V lab strain, although this effect was rather limited.
637 However, potentiation by clomiphene becomes much stronger in amoxicillin-resistant strains such as 19F,
638 Spain-23F and 11A. In *S. pneumoniae*, resistance towards β-lactam antibiotics is mostly caused by mosaic
639 penicillin binding proteins (PBPs). These resistance-conferring mosaic PBPs are formed by recombination
640 events following horizontal gene transfer from β-lactam resistant donor strains[4,7]. We speculate that these
641 mosaic PBPs display suboptimal activity which allows them to remain active during amoxicillin treatment
642 but fail to carry out their task if the amount of peptidoglycan precursors available to them becomes
643 limiting due to a deficiency in Und-P production.
644

645 Whereas this combination treatment strategy works remarkably well *in vitro*, *in vivo* results using a murine
646 pneumonia disease model did not show benefits of combining amoxicillin treatment with clomiphene,
647 likely because the *in vivo* concentration of active clomiphene was too low in the lungs. Nonetheless, we
648 believe that clomiphene represents a promising starting point for the development of an optimized
649 antibacterial compound that can be used in combination with amoxicillin and potentially other β-lactams.
650 Clomiphene is an FDA-approved prodrug that is administered as a racemic mixture of two stereoisomers
651 and is metabolized by the liver into active compounds that stimulate ovulation in anovulatory women[77-
652 79,82]. However, since we observe antibacterial effects and amoxicillin potentiation *in vitro*, it seems likely
653 that one or both of the prodrug isomers exert the desired effect. Determining which clomiphene
654 stereoisomer has the highest antibacterial activity and designing non-metabolizable derivatives that are
655 active at lower concentrations would be the first step to further optimize the here proposed combination
656 treatment strategy for *in vivo* use. We hope that such an optimized antibacterial compound can be
657 exploited for the eradication of amoxicillin-resistant *S. pneumoniae* infections and could potentially also
658 target other species and/or strains with a different resistance profile towards β-lactam antibiotics. We
659 therefore believe that further investigation into this combination treatment strategy holds much promise
660 in combatting the ever-increasing amount of antibiotic-resistant bacterial infections.
661

662 **Materials & Methods**

663

664 **Bacterial strains and growth conditions**

665 All pneumococcal strains used in this work are listed in Table 2. Unless specified otherwise, strains used
666 throughout this work are derivatives of *S. pneumoniae* D39V[49]. In general, genomic changes were
667 introduced by homologous recombination after transformation of a linear DNA molecule into *S.*
668 *pneumoniae*. This linear DNA was either obtained through a one-step PCR reaction starting from a
669 different strain that already carried the desired transformation product (e.g. *hlpA-gfp* and *ftsZ-mCherry*)
670 or through golden gate cloning in which three different PCR products were ligated. The first and last of
671 these PCR products were homologous to the up- and downstream regions of the genome where a deletion
672 or insertion had to be made. In case of insertion of expression cassettes into the *zip* locus, these fragments
673 also contained a P_{lac} promoter and a spectinomycin (or trimethoprim) resistance marker through
674 amplification of fragments of the pPEPZ plasmid[53]. In case of insertion of expression cassettes into the
675 *bgaA* locus, these fragments also contained a P_{tet} promoter and a tetracycline resistance marker through
676 amplification of fragments from strain VL2212[23]. The third, middle fragment contained an antibiotic
677 marker or a sequence to be inserted into the genome. Golden gate cloning sites were introduced into the
678 PCR fragments as part of the primers. PCR fragments were digested with either BsaI, Esp3I or SapI,
679 followed by ligation and transformation. In case individual sgRNAs were cloned into *S. pneumoniae*, the
680 sgRNA sequences were first inserted into the pPEPZ-sgRNAclone plasmid in *E. coli*, as described
681 previously[23]. These integrative plasmids were then transformed into *S. pneumoniae*. Transformation was
682 performed with cells that were made competent by addition of the Competence Stimulating Peptide (CSP-
683 1) using a previously published protocol[83]. Primers that were used for cloning are listed in Table 3. *hlpA-*
684 *gfp* was amplified from VL2226 with primers OVL47&48. *ftsZ-mCherry* was amplified from VL1630 with
685 primers OVL898&901. Both PCR products were transformed to VL1998 to create VL3117.
686 Complementation constructs for mevalonate operon 1 (*mvaS-mvaA*) and operon 2 (*mvk-mvaD-mvaK2-*
687 *fni*) were made by amplification of the corresponding operons using primer pairs OVL3962&63 and
688 OVL3958&59, respectively. Up- and downstream regions for insertion into the *zip* locus were amplified
689 using primer pairs OVL3493&2181 and OVL2182&3496. For the complementation constructs of the *uppS*
690 and *mraY* genes that were amplified using primers OVL4583&84 and OVL4595&96, respectively, up- and
691 downstream regions of the *zip* locus were created using OVL3493&4341 and 2182&3496. The
692 complementation construct for SPV_1620 was created by amplification of the gene using OVL3671&72
693 and up- and downstream *zip* regions were produced using OVL3493&3650 and 3649&3496. Deletion of

694 the corresponding native genes was performed by replacing them with a promoter-less kanamycin
695 resistance cassette that was expressed using the native promoter of the deleted genes. The kanamycin
696 cassette was amplified from the pPEPY plasmid[53] with primers OVL3981&82. The up- and downstream
697 regions of the genes to be deleted were amplified using OVL4069&70 and OVL4071&72 for mevalonate
698 operon 1 (*mvaS-mvaA*), OVL4585&86 and OVL4587&88 for *uppS*, OVL4597&98 and OVL4599&4600 for
699 *mraY* and OVL3677&4601 and OVL 4602&3680 for *SPV_1620*. Due to low expression levels [84], mevalonate
700 operon 2 (*mvk-mvaD-mvaK2-fni*) was replaced with a Km cassette that carried its own constitutive
701 promoter. This fragment was amplified with OVL3983&82 from pPEPY[53] and up- and downstream regions
702 for this operon were amplified with primer pairs OVL4061&62 and OVL4063&64. A complementation
703 construct for *divIVA* was made by amplification of this gene using primers OVL5707 &08. Up- and
704 downstream regions for insertion into the *bgaA* locus were amplified using primer pairs
705 OVL2077&OVL5705 and OVL5706&1369. Deletion of *divIVA* was performed by replacement with a
706 promoter-less chloramphenicol resistance cassette that was expressed using the *divIVA* promoter. The
707 chloramphenicol cassette was amplified from VL3117 with primers OVL5727&28. The up- and
708 downstream regions of *divIVA* were amplified using OV5729&30 and OVL5731&32, respectively. A
709 complementation construct for *pbp2x* was made by amplification of this gene using primers OVL6276&77.
710 Up- and downstream regions for insertion into the *bgaA* locus were amplified using primer pairs
711 OVL2077&OVL5717 and OVL5718&1369. Deletion of *pbp2x* was performed by replacement with a
712 promoter-less erythromycin resistance cassette that was expressed using the *pbp2x* promoter. The
713 cassette was amplified from pJWV502[23] with primers OVL2933&34. The up- and downstream regions of
714 *pbp2x* were amplified using OV6214&15 and OVL6216&17, respectively.
715
716 Strains were grown in liquid C+Y medium (pH = 6.8)[85] at 37°C without shaking under normal atmospheric
717 conditions. Plating was performed inside Columbia agar with 3% sheep blood and plates were incubated
718 at 37°C in a controlled atmosphere containing 5% CO_2.
719
720 Antibiotics for selection were used at the following concentrations: chloramphenicol (Cm) 3 µg/ml,
721 erythromycin (Ery) 0.5 µg/ml, gentamicin (Gm) 40µg/ml, kanamycin (Km) 150 µg/ml, spectinomycin (Spec)
722 100 µg/ml, tetracycline (Tc) 0.5 µg/ml, Trimethoprim (Trm) 10 µg/ml. When necessary, P_{lac} promoters
723 were induced with various amounts of IPTG; 1 mM IPTG for induction of dCas9 for the sCRilecs-seq
724 screens, 20 µM IPTG for complementation of mevalonate operon 1 (*mvaS*, *mvaZ*), 100 µM for
725 complementation of *uppS* and 1 mM IPTG for complementation of mevalonate operon 2 (*mvk*, *mvaD*,

726 *mvaK2*, *fni*), *mraY* or *SPV_1620*. When necessary, P_{tet} promoters were induced with 500 ng/ml
727 anhydrotetracycline (aTc). Where appropriate, mevalonic acid was added to cultures at the concentration
728 indicated in the text (ranging from 100 µM to 1 mM). When strains lacking the first mevalonate operon
729 had to be grown under non-limiting conditions, 1 mM mevalonic acid was used. The concentrations of
730 antibiotics and other compounds that were used to assess their antibacterial activity are indicated in the
731 main text and/or figures and/or figure legends.
732
733 **Table 2: *S. pneumoniae* strains used in this study.**

Strain	Genome	Reference
D39V	Serotype 2, wildtype	[49]
19F	Serotype 19F, clinical isolate	This work
Spain-23F	Serotype 23F, PMEN1, clinical isolate	German National Reference Center for Streptococci
11A	Serotype 11A, PMEN3, clinical isolate	German National Reference Center for Streptococci
VL333	D39V *prs1*::*lacI-tetR-Gm*	Lab collection
VL567	D39V Δ*cps*::*Cm*	[86]
VL1313	11A	[5]
VL1630	D39V *ftsZ-mCherry-Ery bgaA*::P_{zn}-*gfp-stkP*	Lab collection
VL1998	D39V *prs1*::F6-*lacI-Gm bgaA*::P_{lac}-*dCas9-Tc*	[21]
VL2226	D39V *hlpA-gfp-Cm*	[38]
VL3117	VL1998 *hlpA-gfp-Cm ftsZ-mCherry-Ery*	This work
VL3404	VL333 *hlpA-gfp-Cm ftsZ-mCherry-Ery*	This work
VL3565	VL3404 *zip*::P_{lac}-*mvk-mvaD-mvaK2-fni-Spec* Δ*mvk-mvaD-mvaK2-fni*::*Km*	This work
VL3567	VL3404 *zip*::P_{lac}-*mvaS-mvaA-Spec* Δ*mvaS-mvaA*::*Km*	This work
VL3584	VL3404 *zip*::P_{lac}-*uppS-Spec* Δ*uppS*::*Km*	This work
VL3585	VL3404 *zip*::P_{lac}-*mraY-Spec* Δ*mraY*::*Km*	This work
VL3586	VL3404 *zip*::P_{lac}-*SPV_1620-Trm* Δ*SPV_1620*::*Km*	This work
VL3671	VL3117 *zip*::P3-*sgRNA035*	This work
VL3672	VL3117 *zip*::P3-*sgRNA036*	This work
VL3673	VL3117 *zip*::P3-*sgRNA046*	This work
VL3674	VL3117 *zip*::P3-*sgRNA087*	This work
VL3675	VL3117 *zip*::P3-*sgRNA100*	This work
VL3676	VL3117 *zip*::P3-*sgRNA121*	This work
VL3677	VL3117 *zip*::P3-*sgRNA135*	This work
VL3678	VL3117 *zip*::P3-*sgRNA355*	This work
VL3679	VL3117 *zip*::P3-*sgRNA432*	This work
VL3680	VL3117 *zip*::P3-*sgRNA455*	This work
VL3681	VL3117 *zip*::P3-*sgRNA460*	This work
VL3682	VL3117 *zip*::P3-*sgRNA461*	This work
VL3683	VL3117 *zip*::P3-*sgRNA503*	This work
VL3684	VL3117 *zip*::P3-*sgRNA573*	This work

VL3685	VL3117 *zip*::P3-*sgRNA583*	This work
VL3686	VL3117 *zip*::P3-*sgRNA590*	This work
VL3687	VL3117 *zip*::P3-*sgRNA628*	This work
VL3688	VL3117 *zip*::P3-*sgRNA673*	This work
VL3689	VL3117 *zip*::P3-*sgRNA757*	This work
VL3690	VL3117 *zip*::P3-*sgRNA780*	This work
VL3691	VL3117 *zip*::P3-*sgRNA785*	This work
VL3692	VL3117 *zip*::P3-*sgRNA796*	This work
VL3693	VL3117 *zip*::P3-*sgRNA813*	This work
VL3694	VL3117 *zip*::P3-*sgRNA822*	This work
VL3695	VL3117 *zip*::P3-*sgRNA824*	This work
VL3696	VL3117 *zip*::P3-*sgRNA900*	This work
VL3697	VL3117 *zip*::P3-*sgRNA1019*	This work
VL3699	VL3117 *zip*::P3-*sgRNA1064*	This work
VL3700	VL3117 *zip*::P3-*sgRNA1236*	This work
VL3701	VL3117 *zip*::P3-*sgRNA1240*	This work
VL3702	VL333 Δ*mvaS-mvaA*::*Km*	This work
VL3708	VL333 *zip*::P_{lac}-*mvk-mvaD-mvaK2-fni-Spec* Δ*mvk-mvaD-mvaK2-fni*::*Km*	This work
VL3709	VL333 *zip*::P_{lac}-*mvaS-mvaA-Spec* Δ*mvaS-mvaA*::*Km*	This work
VL3710	VL333 *zip*::P_{lac}-*uppS-Spec* Δ*uppS*::*Km*	This work
VL3711	VL333 *zip*::P_{lac}-*mraY-Spec* Δ*mraY*::*Km*	This work
VL3712	VL333 *zip*::P_{lac}-*SPV_1620-Trm* Δ*SPV_1620*::*Km*	This work
VL3834	VL1998 Δ*mvaS-mvaA*::*Km*	This work
VL4273	VL333 *bgaA*::P_{tet}-*pbp2x-Tc* Δ*pbp2x::Ery*	This work
VL4274	VL3709 *bgaA*::P_{tet}-*pbp2x-Tc* Δ*pbp2x::Ery*	This work
LD0001	VL3709 *bgaA*::P_{tet}-*divIVA-Tc* Δ*divIVA::Cm*	This work

Table 3: Primers used in this study.

Primer	Sequence
OVL47	GATTGTAACCGATTCATCTG
OVL48	GGAATGCTTGGTCAAATCTA
OVL898	CCAACAAGCTTCACAAAATAAACCG
OVL901	CTTATCCGTTGCACGCTGACTC
OVL1369	GTCTTCTTTTTTACCTTTAGTAACTACTAATCCTGCAC
OVL2077	ATTCCTTCTTAACGCCCCAAGTTC
OVL2181	GCGTCACGTCTCAGCATTATTTTTCCTCCTTATTTAT
OVL2182	GCGTCACGTCTCACGGATCCCTCCAGTAACTCGAGAA
OVL2933	GATCGGTCTCGAGGAATTTTCATATGAACAAAAATATAAAATATTCTCAA
OVL2934	GATCGGTCTCGTTATTTCCTCCCGTTAAATAATAGATAACTATTAAAAAT
OVL3493	GCCAATAAATTGCTTCCTTGTTTT
OVL3496	ATGACACGGATTTTAAGAATAATTCTTTC
OVL3649	TGTGTGGCTCTTCGAGAACTCGAGAAAAAAAAACCGCGCCC
OVL3650	TGTGTGGCTCTTCGGTTTCATTATTTTTCCTCCTTATTTATTTAGATCTTAATTGTGAGC
OVL3671	CTGGTAGCTCTTCCAACATGCTGAAATGGGAAGACTTGCCTG

OVL3672	CTGGTAGCTCTTCCTCTTTATTTTAGTACCTCAAACACGGTT
OVL3677	GTATAGTAAGCTGGCAGAGAATATC
OVL3680	ATACTTTTTAGGGACAGGATCAC
OVL3958	GCGTCACGTCTCAATGCTCGTCTAGTAAAAGGAAAAAATGACAAAAAAA
OVL3959	GCGTCACGTCTCATCCGTTACGCCTTTTTCATCTGATCATTTG
OVL3962	GCGTCACGTCTCAATGCAGTATAGAACGATTTTTTACATGAATGATAAAACAG
OVL3963	GCGTCACGTCTCATCCGTTATGATCTTAAATTTTCGAGATAGCGCT
OVL3981	GCGTCACGTCTCAATGGCTAAAATGAGAATATCACCGG
OVL3982	GCGTCACGTCTCACTAAAACAATTCATCCAGTAAAATATAATATTTTATTTTCTCC
OVL3983	GCGTCACGTCTCAGAGGACGCGCAAGCTG
OVL4061	CACTACCAATTGGTGAAGTTGCT
OVL4062	GCGTCACGTCTCACCTCTTTTTCCTTTTACTAGACGAAAAAACGTC
OVL4063	GCGTCACGTCTCATTAGGGCGTAACCAGCGCC
OVL4064	TACAGGTACGATGATTTTGGTCGT
OVL4069	AGCTGAAGATAAAGCCTGTAACCA
OVL4070	GCGTCACGTCTCACCATGTAAAAAATCGTTCTATACTATTTTATCACAAATGG
OVL4071	GCGTCACGTCTCATTAGCATAAAAACTCAGACGAATCGGTCT
OVL4072	ACAGCGCCGATTATTTCCTTTG
OVL4341	GCGTCACGTCTCAATTTATTTAGATCTTAATTGTGAGCGCTC
OVL4583	GCGTCACGTCTCAAAATTTTTGAATAGGAATAAGATCATGTTTGGATTTT
OVL4584	GCGTCACGTCTCATCCGCTAAACTCCTCCAAATCGGCG
OVL4585	TCCAGATTTTTCTTATGAGGAAACCTTATT
OVL4586	GCGTCACGTCTCACCATGATCTTATTCCTATTCAAAAATCTATCGTTTCATT
OVL4587	GCGTCACGTCTCATTAGGGAGGAGTTTAGGAGGAAATATGACC
OVL4588	CTGTACTGTCAACTATCATAAAGATAATGGT
OVL4595	GCGTCACGTCTCAAAATATTAACTTTAGGAGACTAATATGTTTATTTCCATCAG
OVL4596	GCGTCACGTCTCATCCGTTACATCAAATACAAAATTGCGAGGGT
OVL4597	AGATTGCTGACGAGAAAAATGGTG
OVL4598	GCGTCACGTCTCACCATATTAGTCTCCTAAAGTTAATGTAATTTTTTTAATGTCC
OVL4599	GCGTCACGTCTCATTAGGAATGGCACCCTGATGTTTCA
OVL4600	AATAAATCATCCATGTTGTTAAAATTATTAAAATTGTTGT
OVL4601	GCGTCACGTCTCACCATGCTGTTCTCCTTTGTTTTTATTATAC
OVL4602	GCGTCACGTCTCATTAGAGTAGTCATAAGAAAATGAGTACAG
OVL5705	GCGTCAGGTCTCAATTTATTTAGATCTACTCTATCAATGATAGAGTTATTATACTCT
OVL5706	GCGTCAGGTCTCAGCGTAAGGAAATCCATTATGTACTATTTCTG
OVL5707	GCGTCAGGTCTCAAAATTTAAGTAAGTGAGGAATAGAATGCCAATTACA
OVL5708	GCGTCAGGTCTCAACGCCTACTTCTGGTTCTTCATACATTGGG
OVL5717	GCGTCACGTCTCAATTTATTTAGATCTACTCTATCAATGATAGAGTTATTATACTCT
OVL5718	GCGTCACGTCTCAGCGTAAGGAAATCCATTATGTACTATTTCTG
OVL5727	GCGTCAGGTCTCAATGAACTTTAATAAAATTGATTTAGACAATTGGAAGAG
OVL5728	GCGTCAGGTCTCATTATAAAAGCCAGTCATTAGGCCTATCT
OVL5729	CTCCTTTTTTAACTCCTTTTATCAATCCTCA
OVL5730	GCGTCAGGTCTCATCATTCTATTCCTCACTTACTTAATAATAACTGGACG
OVL5731	GCGTCAGGTCTCAATAACTCCAGTGCATCCGACAGG
OVL5732	ACCAAGTCCATTTCTTTACGTTTGAC
OVL6214	GCGCGTAAGATTGAGCAA

OVL6215	GATCGGTCTCATCCTATCTTACTCCGCTATTCTAATATTTTCA
OVL6216	GATCGGTCTCGATAAATCAAGGACATTAAAAAAATTACATTAACTT
OVL6217	ACATCACCCATAAAGACCTTG
OVL6276	GCGTCACGTCTCAAAATTTAGAATAGCGGAGTAAGATATGAAGTGG
OVL6277	GCGTCACGTCTCAACGCTTAGTCTCCTAAAGTTAATGTAATTTTTTTAATGTCC

736

737 **Mechanical disruption of *S. pneumoniae* cell chains**

738 Cultures were diluted 3x in PBS to a final volume of 1 ml in screw cap tubes. Tubes were placed into a
739 FastPrep-24™ 5G Instrument (MP Biomedicals) with QuickPrep-3 adapter and shaken with a speed of 6.0
740 m/s for 30 s. This protocol was validated using VL3117 that was grown for 3.5h in C+Y medium. Samples
741 were either subjected to mechanical chain disruption using the FastPrep-24™ 5G or not, after which both
742 samples were analyzed by microscopy and flow cytometry.

743

744 **Construction of the CRISPRi libraries**

745 CRISPRi libraries were constructed by transformation of the desired strains with a pool of 1499 different
746 pPEPZ integrative plasmids carrying constitutively-expressed sgRNA sequences that together target the
747 entire genome[23]. sgRNAs are under control of the constitutive P3 promoter, while the *dcas9* gene is
748 inserted chromosomally under control of the inducible P_{lac} promoter. The 1499 sgRNAs were designed to
749 each target a specific operon. All sgRNA sequences together with their targets and potential off-targets
750 were published previously[23]. For the initial screen, D39V P_{lac}-*dcas9 hlpA-gfp ftsZ-mCherry* (VL3117) was
751 transformed. Our second sCRilecs-seq screen was performed after transformation of D39V P_{lac}-*dcas9*
752 Δ*mvaS* Δ*mvaA* (VL3834) in the presence of 1 mM mevalonic acid. For both libraries, at least 10^5 individual
753 transformants were obtained and collected.

754

755 **sCRilecs-seq screen**

756 The transformed D39V P_{lac}-*dcas9 hlpA-gfp ftsZ-mCherry* (VL3117) library was grown for 3.5h in C+Y
757 medium supplemented with 1 mM IPTG. The D39V P_{lac}-*dcas9* Δ*mvaS* Δ*mvaA* (VL3834) library was grown
758 for 3.5h in C+Y medium supplemented with 1 mM IPTG and 100 µM mevalonic acid. Cell chains were
759 mechanically disrupted (see "Mechanical disruption of *S. pneumoniae* cell chains") and further diluted
760 into PBS 3-10x based on culture density.

761 Cells were sorted using a FACSAria™ IIIu Cell Sorter (BD Biosciences) equipped with violet, blue and red
762 lasers and a 70 µm nozzle. In case of the D39V P_{lac}-*dcas9 hlpA-gfp ftsZ-mCherry* (VL3117) library, cells were
763 gated based on FSC, SSC and GFP fluorescence. For the D39V P_{lac}-*dcas9* Δ*mvaS* Δ*mvaA* (VL3834) library,
764 cells were gated based on FSC and SSC only. For both libraries, cells with the 10% highest and lowest FSC

765 values were collected, as well as 70% of the population located around the median FSC value. For the
766 D39V P_{lac}-*dcas9 hlpA-gfp ftsZ-mCherry* (VL3117) library, the same fractions for GFP and mCherry values
767 were also sorted. Flow rates and dilutions were adjusted to keep the efficiency of sorting as high as
768 possible (and certainly above 85%) while not exceeding a sorting time of 60 min per sample. For every
769 fraction, 1.5 x 10^6 cells were collected and 6 different biological repeats were performed.
770 Cells were collected into 2 ml tubes, centrifuged at 18000 g for 5 min and pellets were stored at -20°C.
771 Cells were lysed by dissolving pellets in 10 µl H_2O + 0.025% DOC + 0.05% SDS and incubating 20 min at
772 37°C, followed by 5 min incubation at 80°C. After samples were allowed to cool off, a colony PCR was
773 performed using primers that contain index and adapter sequences necessary for Illumina sequencing. 10
774 µl of the lysed cell mixture was added to the PCR reaction as input DNA and 30 PCR cycles were performed.
775 The amplicons were purified from a 2% agarose gel and Illumina sequenced on a MiniSeq according to
776 manufacturer's instructions. Sequencing was performed with a custom sequencing protocol[23].
777 Data analysis was performed as described previously[23]. The sgRNA sequences were recovered from the
778 resulting reads using Trimmomatic[87] and mapped onto the *S. pneumoniae* D39V genome using Bowtie2[88].
779 The mapped sgRNAs were counted using featureCounts[89] and the DESeq2 R package was used to define
780 enrichments and associated p values for every sgRNA[90]. For the initial sCRilecs-seq screen, we defined
781 significant hits as sgRNAs from the fraction with the highest or lowest FSC/GFP/mCherry values with an
782 adjusted p value < 0.1 and $Log_2FC > 1$ compared to counts from the corresponding control population. For
783 the second sCRilecs-seq screen performed with a Δ*mvaS-mvaA* mutant limits were set at an adjusted p
784 value < 0.05 and $Log_2FC > 1$.
785

786 **Flow cytometry**

787 Flow cytometry experiments were performed using NovoCyte 2100YB (ACEA Biosciences) flow cytometer
788 equipped with violet, blue and red lasers. To validate sCRilecs-seq hits, strains were grown for 3.5h in C+Y
789 medium with or without 1 mM IPTG. Cultures were diluted in PBS and cell chains were disrupted as
790 described above. Next, cells were incubated for 30 min at room temperature to mimic the average waiting
791 time in the 60 min sorting step before FSC was measured. Cell gatings were chosen based on FSC, SSC and
792 GFP values, as was done during sorting.
793

794 **Gene ontology enrichment analyses**

795 Gene ontology enrichment analyses were performed using the online Gene Ontology Resource platform
796 that is coupled to the PANTHER classification system analysis tool[45-47]. Validated significant sgRNA hits

797 were translated into the spr identifiers that correspond to the targeted genes, which were used as the
798 input gene set that was compared to the *S. pneumoniae* reference list provided by the platform. A
799 PANTHER overrepresentation analysis was performed to identify biological processes that are
800 overrepresented as defined by a Fisher's exact test using FDR-corrected p values. The significance cut-off
801 was set at adjusted p value < 0.05.
802
803 **OD growth curves**
804 Cultures were grown until OD_{595nm} 0.1 in C+Y medium under non-limiting conditions
805 (deletion/complementation strains were grown with the appropriate amount of IPTG, aTc or mevalonic
806 acid, as listed in "Bacterial strains and growth conditions"). Cultures were diluted 100x into C+Y medium
807 supplemented or not with IPTG, aTc or mevalonic acid and with or without the addition of antibacterial
808 compounds, as indicated in the text. 300 µl of cell suspension was transferred into 96-well plates. When
809 growth in the presence of BAL fluid was tested, cultures were diluted 100x into C+Y medium
810 supplemented with ¼ BAL fluid. 200 µl of cell suspension was transferred into 96-well plates. In both cases,
811 addition of compounds such as amoxicillin or clomiphene occurred at this stage by diluting stock
812 concentrations into the wells of the 96-well plates (dilutions were chosen to always keep the DMSO
813 concentrations in the wells ≤ 1%). Growth was monitored by measuring $OD_{595\ nm}$ every 10 min using a
814 TECAN Infinite F200 Pro. OD_{595nm} values were normalized so that the lowest value measured during the
815 first hour of growth was 0.001, the initial OD_{595nm} value of the inoculum. In case the area under the curve
816 needed to be calculated, values were log-transformed before this parameter was determined using
817 GraphPad Prism 9.
818
819 **Minimal Inhibitory Concentration (MIC) measurements**
820 MIC values were determined by constructing growth curves in C+Y medium (see above). The MIC was
821 taken to be the concentration of the tested compound where the maximum OD_{595nm} value obtained was
822 less than 10% of the maximal OD_{595nm} value obtained in the absence of the compound.
823
824 **Phase contrast and fluorescence microscopy**
825 For the determination of cell morphology and FtsZ localization, cultures were grown until $OD_{595\ nm}$ 0.1 in
826 C+Y medium under non-limiting conditions (deletion/complementation strains were grown with the
827 appropriate amount of IPTG or mevalonic acid, as listed in "Bacterial strains and growth conditions").
828 Cultures were then diluted 100x into C+Y medium supplemented or not with IPTG or mevalonic acid and

829 grown until the $OD_{595\ nm}$ of the wild-type strain reached 0.2. At this point, cultures were diluted to $OD_{595\ nm}$
830 of 0.1 and incubated for 45 min at 30°C in order to slow down growth prior to imaging. 1 ml of cell
831 suspension was spun down (10000 g for 2 min) and pellets were dissolved in 40 µl PBS. Cells were kept on
832 ice prior to imaging.
833 To investigate peptidoglycan production using FDAAs, cultures were grown until $OD_{595\ nm}$ 0.1 in C+Y
834 medium under non-limiting conditions (deletion/complementation strains were grown with the
835 appropriate amount of IPTG, as listed in "Bacterial strains and growth conditions"). Cultures were then
836 diluted 100x into C+Y medium without IPTG and grown until the $OD_{595\ nm}$ of the wild-type strain reached
837 0.1. At this point, 250 µM sBADA was added and cultures were incubated for 15 min at 37°C. Cells were
838 washed 3 times with cold PBS (centrifuge at 10000 g for 1 min at 4°C) and pellets were dissolved in C+Y
839 medium containing 250 µM RADA. After incubating cells for 15 min at 37°C, the three wash steps were
840 repeated. Pellets were dissolved in PBS and kept on ice prior to imaging.
841 Cells were imaged by placing 0.4 µl of cell suspension on pads made of PBS containing 1% agarose. Imaging
842 was performed using a Leica DMi8 microscope with a sCMOS DFC9000 (Leica) camera and a SOLA light
843 engine (Lumencor). Phase contrast images were acquired using transmission light with 100 ms exposure
844 time. Leica DMi8 filter sets were used as follows: mCherry (Chroma 49017, Ex: 560/40 nm, BS: LP 590 nm,
845 Em: LP 590 nm) with exposure time 700 msec, sBADA (Ex: 470/40 nm Chroma ET470/40x, BS: LP 498 Leica
846 11536022, Em: 520/40 nm Chroma ET520/40m) with exposure time 200 msec, and RADA (Chroma 49017,
847 Ex: 560/40 nm, BS: LP 590 nm, Em: LP 590 nm) with exposure time 100 msec. Images were processed
848 using ImageJ and deconvolution was performed using Huygens software (Scientific Volume Imaging) with
849 standard settings using 15 iterations for FtsZ-mCherry and sBADA and 25 iterations for RADA.
850 Quantification of cell length and other properties was done using MicrobeJ[91] and BactMAP[92].
851 For the analysis and statistical comparison of cell size across different mutants and conditions (Figure 1C;
852 Figure 3D, F and H; Figure S2A-C; Figure 5J; Figure 6A), the following approach was used[93]. For every
853 mutant and/or condition, cell size was recorded for at least 3 biologically independent repeats. The one
854 exception is the depletion of *mraY* at time point 4.5h where only 2 independent repeats could be analyzed.
855 At this late time point, the culture is most often taken over by suppressor mutants with normal
856 morphology. Despite many attempts, we failed to obtain a third repeat in which the *mraY* depletion
857 phenotype was still apparent. For every repeat, at least 100 cells were recorded unless mentioned
858 otherwise and their average cell length was determined. These average cell lengths were used to calculate
859 the mean and SEM values that are shown in the main figures. The average cell lengths of each repeat were

860 also used to determine any statistically significant differences using a Wilcox test with FDR corrected p
861 values.
862
863 **Transmission electron microscopy**
864 Cultures were grown until $OD_{595\ nm}$ 0.1 in C+Y medium under non-limiting conditions
865 (deletion/complementation strains were grown with the appropriate amount of IPTG, as listed in
866 "Bacterial strains and growth conditions"). Cultures were then diluted 100x into C+Y medium without IPTG
867 and grown until the $OD_{595\ nm}$ of the wild-type strain reached 0.2. At this point, cultures were diluted to
868 $OD_{595\ nm}$ of 0.1 and incubated for 45 min at 30°C in order to slow down growth prior to imaging. 4 ml of
869 cell suspension was spun down at 10000 g and pellets were fixed in glutaraldehyde solution 2.5% (EMS)
870 and in osmium tetroxide 1% (EMS) with 1.5% of potassium ferrocyanide (Sigma) in phosphate buffer (PB
871 0.1 M [pH 7.4]) for 1h at room temperature. Samples were washed twice with H_2O and pellets were
872 embedded in agarose 2% (Sigma) in water, dehydrated in acetone solution (Sigma) at graded
873 concentrations (30% - 40 min; 70% - 40 min; 100% - 2x1h). This was followed by infiltration in Epon resin
874 (EMS) at graded concentrations (Epon 33% in acetone - 2h; Epon 66% in acetone - 4h; Epon 100% - 2x8h)
875 and finally polymerized for 48h at 60°C. Ultrathin sections of 50 nm thick were cut using a Leica Ultracut
876 (Leica Mikrosysteme GmbH), picked up on a copper slot grid 2x1mm (EMS) coated with a polystyrene film
877 (Sigma). Sections were post-stained with uranyl acetate (Sigma) 4% in H_2O for 10 min, rinsed several times
878 with H_2O followed by Reynolds lead citrate in H_2O (Sigma) for 10 min and rinsed several times with H_2O.
879 Micrographs were taken with a transmission electron microscope FEI CM100 (FEI) at an acceleration
880 voltage of 80 kV with a TVIPS TemCamF416 digital camera (TVIPS GmbH).
881
882 ***In vivo* experiments using a murine pneumonia disease model**
883 Male C57BL/6JRj mice (8 weeks old) (Janvier Laboratories, Saint Berthevin, France) were maintained in
884 individually ventilated cages and were handled in a vertical laminar flow cabinet (class II A2, ESCO,
885 Hatboro, PA). All experiments complied with national, institutional and European regulations and ethical
886 guidelines, were approved by our Institutional Animal Care and Use guidelines (D59-350009, Institut
887 Pasteur de Lille; Protocol APAFIS#16966 201805311410769_v3) and were conducted by qualified,
888 accredited personnel.
889 Mice were anesthetized by intraperitoneal injection of 1.25 mg (50 mg/kg) ketamine plus 0.25 mg (10
890 mg/kg) xylazine in 200 µl of PBS. Mice were infected intranasally with 30 µl of PBS containing 50 plaque-
891 forming units (PFUs) of the pathogenic murine-adapted H3N2 influenza A virus strain Scotland/20/74[76].

892 Seven days later, mice were inoculated intranasally with 10^5 CFU of *S. pneumoniae* strain 19F in 30 µl of
893 PBS. Mice were treated intragastrically with 5 mg of clomiphene (Clomid, Sanofi-Aventis, France) in 200
894 µl of water and or 1 mg of amoxicillin (Clamoxyl for injection, GlaxoSmithKline) in 200 µl of water at 8 and
895 12 hours post-infection, respectively. Mice were sacrificed 24 hours post-infection by intraperitoneal
896 injection of 5.47 mg of sodium pentobarbital in 100 µl PBS (Euthasol, Virbac, France). Bronchoalveolar
897 lavage fluids (BAL) were sampled after intratracheal injection of 1 mL of PBS and centrifugation at 1400
898 rpm for 10 min. Lungs and spleen were sampled to determine the bacterial load. Tissues were
899 homogenized with an UltraTurrax homogenizer (IKA-Werke, Staufen, Germany) and serial dilutions were
900 plated on blood agar plates and incubated at 37°C. Viable counts were determined 24h later. Statistical
901 significance between groups was calculated by the Kruskall-Wallis test (One-Way ANOVA). Analyses were
902 performed with Prism software (version 9, GraphPad Software, La Jolla, CA).
903
904 **Acknowledgements**
905 We thank Mark van der Linden, German National Reference Center for Streptococci for providing us with
906 the *S. pneumoniae* clinical isolates of Spain-23F and 11A strains and Frédéric Wallet, Regional Reference
907 Center for pneumococci, Lille, for providing the *S. pneumoniae* strain 19F. We are thankful to the electron
908 microscopy facility of the university of Lausanne for their assistance in obtaining TEM images. We thank
909 Emanuele Cattani for technical assistance, construction of strains VL3710, VL3711 and VL3712, and
910 microscopy data used in Figure S2B-C. Work in the Veening lab is supported by the Swiss National Science
911 Foundation (SNSF) (project grants 310030_200792 and 310030_192517), SNSF JPIAMR grant
912 (40AR40_185533), SNSF NCCR 'AntiResist' (51NF40_180541) and ERC consolidator grant 771534-
913 PneumoCaTChER. LD is the recipient of a Marie Skłodowska Curie Actions – Individual Fellowship (MSCA-
914 IF, proposal number 837923). JCS, MB, and CC received funding from Région Hauts de France STaRS, and
915 the European Union's Horizon 2020 research and innovation programme under grant agreement No
916 847786.
917

918 **References**

919 1 Weiser, J. N., Ferreira, D. M. & Paton, J. C. *Streptococcus pneumoniae*: transmission, colonization
920 and invasion. *Nat Rev Microbiol* **16**, 355-367, doi:10.1038/s41579-018-0001-8 (2018).
921 2 O'Brien, K. L. *et al.* Burden of disease caused by *Streptococcus pneumoniae* in children younger
922 than 5 years: global estimates. *Lancet* **374**, 893-902, doi:10.1016/S0140-6736(09)61204-6
923 (2009).
924 3 Bogaert, D., De Groot, R. & Hermans, P. W. *Streptococcus pneumoniae* colonisation: the key to
925 pneumococcal disease. *Lancet Infect Dis* **4**, 144-154, doi:10.1016/S1473-3099(04)00938-7
926 (2004).
927 4 Jensen, A., Valdorsson, O., Frimodt-Moller, N., Hollingshead, S. & Kilian, M. Commensal
928 streptococci serve as a reservoir for beta-lactam resistance genes in *Streptococcus pneumoniae*.
929 *Antimicrob Agents Chemother* **59**, 3529-3540, doi:10.1128/AAC.00429-15 (2015).
930 5 Camara, J. *et al.* Evolution of the beta-lactam-resistant *Streptococcus pneumoniae* PMEN3 clone
931 over a 30 year period in Barcelona, Spain. *J Antimicrob Chemother* **73**, 2941-2951,
932 doi:10.1093/jac/dky305 (2018).
933 6 Schrag, S. J. *et al.* Emergence of *Streptococcus pneumoniae* with very-high-level resistance to
934 penicillin. *Antimicrob Agents Chemother* **48**, 3016-3023, doi:10.1128/AAC.48.8.3016-3023.2004
935 (2004).
936 7 Hakenbeck, R., Bruckner, R., Denapaite, D. & Maurer, P. Molecular mechanisms of beta-lactam
937 resistance in *Streptococcus pneumoniae*. *Future Microbiol* **7**, 395-410, doi:10.2217/fmb.12.2
938 (2012).
939 8 Kaur, R., Casey, J. R. & Pichichero, M. E. Emerging *Streptococcus pneumoniae* strains colonizing
940 the nasopharynx in children after 13-valent pneumococcal conjugate vaccination in comparison
941 to the 7-valent era, 2006-2015. *Pediatr Infect Dis J* **35**, 901-906,
942 doi:10.1097/INF.0000000000001206 (2016).
943 9 Brueggemann, A. B., Pai, R., Crook, D. W. & Beall, B. Vaccine escape recombinants emerge after
944 pneumococcal vaccination in the United States. *PLoS Pathog* **3**, e168,
945 doi:10.1371/journal.ppat.0030168 (2007).
946 10 Hanage, W. P., Fraser, C., Tang, J., Connor, T. R. & Corander, J. Hyper-recombination, diversity,
947 and antibiotic resistance in pneumococcus. *Science* **324**, 1454-1457,
948 doi:10.1126/science.1171908 (2009).
949 11 Domenech, A. *et al.* Proton motive force disruptors block bacterial competence and horizontal
950 gene transfer. *Cell Host Microbe* **27**, 544-555 e543, doi:10.1016/j.chom.2020.02.002 (2020).
951 12 Chi, F., Nolte, O., Bergmann, C., Ip, M. & Hakenbeck, R. Crossing the barrier: evolution and
952 spread of a major class of mosaic *pbp2x* in *Streptococcus pneumoniae*, *S. mitis* and *S. oralis*. *Int J*
953 *Med Microbiol* **297**, 503-512, doi:10.1016/j.ijmm.2007.02.009 (2007).
954 13 Prieto, J., Calvo, A. & Gomez-Lus, M. L. Antimicrobial resistance: a class effect? *J Antimicrob*
955 *Chemother* **50 Suppl S2**, 7-12, doi:10.1093/jac/dkf508 (2002).
956 14 Baquero, F., Baquero-Artigao, G., Canton, R. & Garcia-Rey, C. Antibiotic consumption and
957 resistance selection in *Streptococcus pneumoniae*. *J Antimicrob Chemother* **50 Suppl S2**, 27-37,
958 doi:10.1093/jac/dkf504 (2002).
959 15 Jacobs, M. R. Building in efficacy: developing solutions to combat drug-resistant *S. pneumoniae*.
960 *Clin Microbiol Infect* **10 Suppl 2**, 18-27, doi:10.1111/j.1470-9465.2004.00862.x (2004).
961 16 Bradley, J. S. *et al.* The management of community-acquired pneumonia in infants and children
962 older than 3 months of age: clinical practice guidelines by the Pediatric Infectious Diseases
963 Society and the Infectious Diseases Society of America. *Clin Infect Dis* **53**, e25-76,
964 doi:10.1093/cid/cir531 (2011).

965 17 Thiem, U., Heppner, H. J. & Pientka, L. Elderly patients with community-acquired pneumonia:
966 optimal treatment strategies. *Drugs Aging* **28**, 519-537, doi:10.2165/11591980-000000000-
967 00000 (2011).
968 18 Qi, L. S. *et al.* Repurposing CRISPR as an RNA-guided platform for sequence-specific control of
969 gene expression. *Cell* **152**, 1173-1183, doi:10.1016/j.cell.2013.02.022 (2013).
970 19 Peters, J. M. *et al.* A comprehensive, CRISPR-based functional analysis of essential genes in
971 bacteria. *Cell* **165**, 1493-1506, doi:10.1016/j.cell.2016.05.003 (2016).
972 20 Bikard, D. *et al.* Programmable repression and activation of bacterial gene expression using an
973 engineered CRISPR-Cas system. *Nucleic Acids Res* **41**, 7429-7437, doi:10.1093/nar/gkt520
974 (2013).
975 21 Liu, X. *et al.* High-throughput CRISPRi phenotyping identifies new essential genes in
976 *Streptococcus pneumoniae*. *Mol Syst Biol* **13**, 931, doi:10.15252/msb.20167449 (2017).
977 22 Cui, L. *et al.* A CRISPRi screen in *E. coli* reveals sequence-specific toxicity of dCas9. *Nat Commun*
978 **9**, 1912, doi:10.1038/s41467-018-04209-5 (2018).
979 23 Liu, X. *et al.* Exploration of bacterial bottlenecks and *Streptococcus pneumoniae* pathogenesis by
980 CRISPRi-Seq. *Cell Host Microbe* **29**, 107-120 e106, doi:10.1016/j.chom.2020.10.001 (2021).
981 24 de Wet, T. J., Gobe, I., Mhlanga, M. M. & Warner, D. F. CRISPRi-Seq for the identification and
982 characterisation of essential Mycobacterial genes and transcriptional units. *BioRxiv*, 358275,
983 doi:https://doi.org/10.1101/358275 (2018).
984 25 Lee, H. H. *et al.* Functional genomics of the rapidly replicating bacterium *Vibrio natriegens* by
985 CRISPRi. *Nat Microbiol* **4**, 1105-1113, doi:10.1038/s41564-019-0423-8 (2019).
986 26 Rousset, F. *et al.* Genome-wide CRISPR-dCas9 screens in *E. coli* identify essential genes and
987 phage host factors. *PLoS Genet* **14**, e1007749, doi:10.1371/journal.pgen.1007749 (2018).
988 27 Wang, T. *et al.* Pooled CRISPR interference screening enables genome-scale functional genomics
989 study in bacteria with superior performance. *Nat Commun* **9**, 2475, doi:10.1038/s41467-018-
990 04899-x (2018).
991 28 Park, J. S. *et al.* A FACS-based genome-wide CRISPR screen reveals a requirement for COPI in
992 *Chlamydia trachomatis* invasion. *iScience* **11**, 71-84, doi:10.1016/j.isci.2018.12.011 (2019).
993 29 Smith, L. M., Jackson, S. A., Gardner, P. P. & Fineran, P. C. SorTn-seq: a high-throughput
994 functional genomics approach to discovering regulators of bacterial gene expression. *Nat*
995 *Protoc*, doi:10.1038/s41596-021-00582-6 (2021).
996 30 Boronat, A. & Rodriguez-Concepcion, M. Terpenoid biosynthesis in prokaryotes. *Adv Biochem*
997 *Eng Biotechnol* **148**, 3-18, doi:10.1007/10_2014_285 (2015).
998 31 Heuston, S., Begley, M., Gahan, C. G. M. & Hill, C. Isoprenoid biosynthesis in bacterial pathogens.
999 *Microbiology (Reading)* **158**, 1389-1401, doi:10.1099/mic.0.051599-0 (2012).
1000 32 Bouhss, A., Trunkfield, A. E., Bugg, T. D. & Mengin-Lecreulx, D. The biosynthesis of peptidoglycan
1001 lipid-linked intermediates. *FEMS Microbiol Rev* **32**, 208-233, doi:10.1111/j.1574-
1002 6976.2007.00089.x (2008).
1003 33 Farha, M. A. *et al.* Antagonism screen for inhibitors of bacterial cell wall biogenesis uncovers an
1004 inhibitor of undecaprenyl diphosphate synthase. *Proc Natl Acad Sci U S A* **112**, 11048-11053,
1005 doi:10.1073/pnas.1511751112 (2015).
1006 34 Tsui, H. T. *et al.* Pbp2x localizes separately from Pbp2b and other peptidoglycan synthesis
1007 proteins during later stages of cell division of *Streptococcus pneumoniae* D39. *Mol Microbiol* **94**,
1008 21-40, doi:10.1111/mmi.12745 (2014).
1009 35 Sorg, R. A. & Veening, J. W. Microscale insights into pneumococcal antibiotic mutant selection
1010 windows. *Nat Commun* **6**, 8773, doi:10.1038/ncomms9773 (2015).
1011 36 Brochado, A. R. *et al.* Species-specific activity of antibacterial drug combinations. *Nature* **559**,
1012 259-263, doi:10.1038/s41586-018-0278-9 (2018).

1013 37 Shi, H. *et al.* Deep phenotypic mapping of bacterial cytoskeletal mutants reveals physiological
1014 robustness to cell size. *Curr Biol* **27**, 3419-3429 e3414, doi:10.1016/j.cub.2017.09.065 (2017).
1015 38 Kjos, M. *et al.* Bright fluorescent *Streptococcus pneumoniae* for live-cell imaging of host-
1016 pathogen interactions. *J Bacteriol* **197**, 807-818, doi:10.1128/JB.02221-14 (2015).
1017 39 Beilharz, K., van Raaphorst, R., Kjos, M. & Veening, J. W. Red fluorescent proteins for gene
1018 expression and protein localization studies in *Streptococcus pneumoniae* and efficient
1019 transformation with DNA assembled via the Gibson Assembly method. *Appl Environ Microbiol*
1020 **81**, 7244-7252, doi:10.1128/AEM.02033-15 (2015).
1021 40 Massidda, O., Novakova, L. & Vollmer, W. From models to pathogens: how much have we
1022 learned about *Streptococcus pneumoniae* cell division? *Environ Microbiol* **15**, 3133-3157,
1023 doi:10.1111/1462-2920.12189 (2013).
1024 41 Rued, B. E. *et al.* Suppression and synthetic-lethal genetic relationships of Δ*gpsB* mutations
1025 indicate that GpsB mediates protein phosphorylation and penicillin-binding protein interactions
1026 in *Streptococcus pneumoniae* D39. *Mol Microbiol* **103**, 931-957, doi:10.1111/mmi.13613 (2017).
1027 42 Land, A. D. *et al.* Requirement of essential Pbp2x and GpsB for septal ring closure in
1028 *Streptococcus pneumoniae* D39. *Mol Microbiol* **90**, 939-955, doi:10.1111/mmi.12408 (2013).
1029 43 Vollmer, W., Massidda, O. & Tomasz, A. The cell wall of *Streptococcus pneumoniae*. *Microbiol*
1030 *Spectr* **7**, GPP3-0018-2018, doi:10.1128/microbiolspec.GPP3-0018-2018 (2019).
1031 44 Brown, S., Santa Maria, J. P., Jr. & Walker, S. Wall teichoic acids of Gram-positive bacteria. *Annu*
1032 *Rev Microbiol* **67**, 313-336, doi:10.1146/annurev-micro-092412-155620 (2013).
1033 45 Ashburner, M. *et al.* Gene ontology: tool for the unification of biology. *Nat Genet* **25**, 25-29,
1034 doi:10.1038/75556 (2000).
1035 46 Mi, H., Muruganujan, A., Ebert, D., Huang, X. & Thomas, P. D. PANTHER version 14: more
1036 genomes, a new PANTHER GO-slim and improvements in enrichment analysis tools. *Nucleic*
1037 *Acids Res* **47**, 419-426, doi:10.1093/nar/gky1038 (2019).
1038 47 Consortium, T. G. O. The Gene Ontology Resource: 20 years and still GOing strong. *Nucleic Acids*
1039 *Res* **47**, 330-338, doi:10.1093/nar/gky1055 (2019).
1040 48 Wilding, E. I. *et al.* Identification, evolution, and essentiality of the mevalonate pathway for
1041 isopentenyl diphosphate biosynthesis in Gram-positive cocci. *J Bacteriol* **182**, 4319-4327,
1042 doi:10.1128/jb.182.15.4319-4327.2000 (2000).
1043 49 Slager, J., Aprianto, R. & Veening, J. W. Deep genome annotation of the opportunistic human
1044 pathogen *Streptococcus pneumoniae* D39. *Nucleic Acids Res* **46**, 9971-9989,
1045 doi:10.1093/nar/gky725 (2018).
1046 50 Balibar, C. J., Shen, X. Y. & Tao, J. S. The mevalonate pathway of *Staphylococcus aureus*. *J*
1047 *Bacteriol* **191**, 851-861, doi:10.1128/Jb.01357-08 (2009).
1048 51 Yu, W. Q. *et al.* The mevalonate auxotrophic mutant of *Staphylococcus aureus* can adapt to
1049 mevalonate depletion. *Antimicrob Agents Ch* **57**, 5710-5713, doi:10.1128/Aac.00726-13 (2013).
1050 52 Reichert, S. *et al.* Genetic adaptation of a mevalonate pathway deficient mutant in
1051 *Staphylococcus aureus*. *Front Microbiol* **9**, 1539, doi:ARTN 1539
1052 10.3389/fmicb.2018.01539 (2018).
1053 53 Keller, L. E., Rueff, A. S., Kurushima, J. & Veening, J. W. Three new integration vectors and
1054 fluorescent proteins for use in the opportunistic human pathogen *Streptococcus pneumoniae*.
1055 *Genes (Basel)* **10**, 394, doi:10.3390/genes10050394 (2019).
1056 54 Kuru, E., Tekkam, S., Hall, E., Brun, Y. V. & Van Nieuwenhze, M. S. Synthesis of fluorescent D-
1057 amino acids and their use for probing peptidoglycan synthesis and bacterial growth *in situ*. *Nat*
1058 *Protoc* **10**, 33-52, doi:10.1038/nprot.2014.197 (2015).

1059 55 Wheeler, R., Mesnage, S., Boneca, I. G., Hobbs, J. K. & Foster, S. J. Super-resolution microscopy
1060 reveals cell wall dynamics and peptidoglycan architecture in ovococcal bacteria. *Mol Microbiol*
1061 **82**, 1096-1109, doi:10.1111/j.1365-2958.2011.07871.x (2011).
1062 56 Yao, Z., Kahne, D. & Kishony, R. Distinct single-cell morphological dynamics under beta-lactam
1063 antibiotics. *Mol Cell* **48**, 705-712, doi:10.1016/j.molcel.2012.09.016 (2012).
1064 57 Yother, J. Capsules of *Streptococcus pneumoniae* and other bacteria: paradigms for
1065 polysaccharide biosynthesis and regulation. *Annu Rev Microbiol* **65**, 563-581,
1066 doi:10.1146/annurev.micro.62.081307.162944 (2011).
1067 58 Barendt, S. M. *et al.* Influences of capsule on cell shape and chain formation of wild-type and
1068 *pcsB* mutants of serotype 2 *Streptococcus pneumoniae*. *J Bacteriol* **191**, 3024-3040,
1069 doi:10.1128/JB.01505-08 (2009).
1070 59 Denapaite, D., Bruckner, R., Hakenbeck, R. & Vollmer, W. Biosynthesis of teichoic acids in
1071 *Streptococcus pneumoniae* and closely related species: lessons from genomes. *Microb Drug*
1072 *Resist* **18**, 344-358, doi:10.1089/mdr.2012.0026 (2012).
1073 60 Beilharz, K. *et al.* Control of cell division in *Streptococcus pneumoniae* by the conserved Ser/Thr
1074 protein kinase StkP. *Proc Natl Acad Sci U S A* **109**, E905-913, doi:10.1073/pnas.1119172109
1075 (2012).
1076 61 Fleurie, A. *et al.* Mutational dissection of the S/T-kinase StkP reveals crucial roles in cell division
1077 of *Streptococcus pneumoniae*. *Mol Microbiol* **83**, 746-758, doi:10.1111/j.1365-
1078 2958.2011.07962.x (2012).
1079 62 Fleurie, A. *et al.* Interplay of the serine/threonine-kinase StkP and the paralogs DivIVA and GpsB
1080 in pneumococcal cell elongation and division. *PLoS Genet* **10**, e1004275,
1081 doi:10.1371/journal.pgen.1004275 (2014).
1082 63 Novakova, L. *et al.* Identification of multiple substrates of the StkP Ser/Thr protein kinase in
1083 *Streptococcus pneumoniae*. *J Bacteriol* **192**, 3629-3638, doi:10.1128/JB.01564-09 (2010).
1084 64 Cho, H. *et al.* Bacterial cell wall biogenesis is mediated by SEDS and PBP polymerase families
1085 functioning semi-autonomously. *Nat Microbiol* **1**, 16172, doi:10.1038/nmicrobiol.2016.172
1086 (2016).
1087 65 Meeske, A. J. *et al.* SEDS proteins are a widespread family of bacterial cell wall polymerases.
1088 *Nature* **537**, 634-638, doi:10.1038/nature19331 (2016).
1089 66 Taguchi, A. *et al.* FtsW is a peptidoglycan polymerase that is functional only in complex with its
1090 cognate penicillin-binding protein. *Nat Microbiol* **4**, 587-594, doi:10.1038/s41564-018-0345-x
1091 (2019).
1092 67 Tsui, H. C. *et al.* Suppression of a deletion mutation in the gene encoding essential PBP2b reveals
1093 a new lytic transglycosylase involved in peripheral peptidoglycan synthesis in *Streptococcus*
1094 *pneumoniae* D39. *Mol Microbiol* **100**, 1039-1065, doi:10.1111/mmi.13366 (2016).
1095 68 Perez, A. J. *et al.* Movement dynamics of divisome proteins and PBP2x:FtsW in cells of
1096 *Streptococcus pneumoniae*. *Proc Natl Acad Sci U S A* **116**, 3211-3220,
1097 doi:10.1073/pnas.1816018116 (2019).
1098 69 Berg, K. H., Stamsas, G. A., Straume, D. & Havarstein, L. S. Effects of low PBP2b levels on cell
1099 morphology and peptidoglycan composition in *Streptococcus pneumoniae* R6. *J Bacteriol* **195**,
1100 4342-4354, doi:10.1128/JB.00184-13 (2013).
1101 70 Kocaoglu, O., Tsui, H. C., Winkler, M. E. & Carlson, E. E. Profiling of beta-lactam selectivity for
1102 penicillin-binding proteins in *Streptococcus pneumoniae* D39. *Antimicrob Agents Chemother* **59**,
1103 3548-3555, doi:10.1128/AAC.05142-14 (2015).
1104 71 Masadeh, M., Mhaidat, N., Alzoubi, K., Al-Azzam, S. & Alnasser, Z. Antibacterial activity of
1105 statins: a comparative study of atorvastatin, simvastatin, and rosuvastatin. *Ann Clin Microbiol*
1106 *Antimicrob* **11**, 13, doi:10.1186/1476-0711-11-13 (2012).

1107 72 Bergman, P. *et al.* Studies on the antibacterial effects of statins - *in vitro* and *in vivo*. *PLoS One* **6**,
1108 e24394, doi:10.1371/journal.pone.0024394 (2011).
1109 73 Kaneko, M., Togashi, N., Hamashima, H., Hirohara, M. & Inoue, Y. Effect of farnesol on
1110 mevalonate pathway of *Staphylococcus aureus*. *J Antibiot (Tokyo)* **64**, 547-549,
1111 doi:10.1038/ja.2011.49 (2011).
1112 74 Imohl, M., Reinert, R. R. & van der Linden, M. Serotype-specific penicillin resistance of
1113 *Streptococcus pneumoniae* in Germany from 1992 to 2008. *Int J Med Microbiol* **300**, 324-330,
1114 doi:10.1016/j.ijmm.2009.11.004 (2010).
1115 75 EUCAST. Breakpoint tables for interpretation of MICs and zone diameters, version 11.0.
1116 http://www.eucast.org/clinical_breakpoints/ (2021).
1117 76 Matarazzo, L. *et al.* Therapeutic synergy between antibiotics and pulmonary Toll-like receptor 5
1118 stimulation in antibiotic-sensitive or -resistant pneumonia. *Front Immunol* **10**, 723,
1119 doi:10.3389/fimmu.2019.00723 (2019).
1120 77 Dickey, R. P. & Holtkamp, D. E. Development, pharmacology and clinical experience with
1121 clomiphene citrate. *Hum Reprod Update* **2**, 483-506, doi:10.1093/humupd/2.6.483 (1996).
1122 78 Huppert, L. C. Induction of ovulation with clomiphene citrate. *Fertil Steril* **31**, 1-8,
1123 doi:10.1016/s0015-0282(16)43749-0 (1979).
1124 79 Nasseri, S. & Ledger, W. L. Clomiphene citrate in the twenty-first century. *Hum Fertil (Camb)* **4**,
1125 145-151, doi:10.1080/1464727012000199212 (2001).
1126 80 Cleverley, R. M. *et al.* The cell cycle regulator GpsB functions as cytosolic adaptor for multiple
1127 cell wall enzymes. *Nat Commun* **10**, 261, doi:10.1038/s41467-018-08056-2 (2019).
1128 81 Zucchini, L. *et al.* PASTA repeats of the protein kinase StkP interconnect cell constriction and
1129 separation of *Streptococcus pneumoniae*. *Nat Microbiol* **3**, 197-209, doi:10.1038/s41564-017-
1130 0069-3 (2018).
1131 82 Murdter, T. E. *et al.* Genetic polymorphism of cytochrome P450 2D6 determines oestrogen
1132 receptor activity of the major infertility drug clomiphene via its active metabolites. *Hum Mol*
1133 *Genet* **21**, 1145-1154, doi:10.1093/hmg/ddr543 (2012).
1134 83 Synefiaridou, D. & Veening, J.-W. Harnessing CRISPR-Cas9 for genome editing in *Streptococcus*
1135 *pneumoniae* D39V. *Appl Environ Microbiol* **87**, e02762-02720, doi:10.1101/2020.06.13.149682
1136 %J bioRxiv (2020).
1137 84 Aprianto, R., Slager, J., Holsappel, S. & Veening, J. W. High-resolution analysis of the
1138 pneumococcal transcriptome under a wide range of infection-relevant conditions. *Nucleic Acids*
1139 *Res* **46**, 9990-10006, doi:10.1093/nar/gky750 (2018).
1140 85 Domenech, A., Slager, J. & Veening, J. W. Antibiotic-induced cell chaining triggers pneumococcal
1141 competence by reshaping quorum sensing to autocrine-like signaling. *Cell Rep* **25**, 2390-2400
1142 e2393, doi:10.1016/j.celrep.2018.11.007 (2018).
1143 86 Moreno-Gamez, S. *et al.* Quorum sensing integrates environmental cues, cell density and cell
1144 history to control bacterial competence. *Nat Commun* **8**, 854, doi:10.1038/s41467-017-00903-y
1145 (2017).
1146 87 Bolger, A. M., Lohse, M. & Usadel, B. Trimmomatic: a flexible trimmer for Illumina sequence
1147 data. *Bioinformatics* **30**, 2114-2120, doi:10.1093/bioinformatics/btu170 (2014).
1148 88 Langmead, B. & Salzberg, S. L. Fast gapped-read alignment with Bowtie 2. *Nat Methods* **9**, 357-
1149 359, doi:10.1038/nmeth.1923 (2012).
1150 89 Liao, Y., Smyth, G. K. & Shi, W. featureCounts: an efficient general purpose program for
1151 assigning sequence reads to genomic features. *Bioinformatics* **30**, 923-930,
1152 doi:10.1093/bioinformatics/btt656 (2014).
1153 90 Love, M. I., Huber, W. & Anders, S. Moderated estimation of fold change and dispersion for
1154 RNA-seq data with DESeq2. *Genome Biol* **15**, 550, doi:10.1186/s13059-014-0550-8 (2014).

1155 91 Ducret, A., Quardokus, E. M. & Brun, Y. V. MicrobeJ, a tool for high throughput bacterial cell
1156 detection and quantitative analysis. *Nat Microbiol* **1**, 16077, doi:10.1038/nmicrobiol.2016.77
1157 (2016).
1158 92 van Raaphorst, R., Kjos, M. & Veening, J. W. BactMAP: An R package for integrating, analyzing
1159 and visualizing bacterial microscopy data. *Mol Microbiol* **113**, 297-308, doi:10.1111/mmi.14417
1160 (2020).
1161 93 Lord, S. J., Velle, K. B., Mullins, R. D. & Fritz-Laylin, L. K. SuperPlots: Communicating
1162 reproducibility and variability in cell biology. *J Cell Biol* **219**, e202001064,
1163 doi:10.1083/jcb.202001064 (2020).
1164